uOttawa

An Automated Approach to Mapping Ocean Front Features Using Sentinel-1 with examples from the Gulf Stream and Agulhas Current

Andrew Newall

Thesis submitted to the
University of Ottawa in partial fulfillment of the requirements for the M.Sc.
Degree in Geography

Department of Geography, Environment and Geomatics
Faculty of Arts
University of Ottawa

Supervisor:

Dr. Anders Knudby

Thesis Committee:

Dr. Michael Sawada

Dr. Wesley Van Wychen

Abstract

This study examines the efficacy of Sentinel-1 Radial Velocity (RVL) imagery at determining the position of ocean current front features, using the Gulf Stream (GS) and Agulhas Current (AC) as case studies. Fronts derived from RVL imagery are compared to fronts derived from Sea Surface Temperature (SST) imagery, specifically Multi-scale Ultra-high Resolution Sea Surface Temperature Analysis (MURSST) data. In the case of the GS, front locations from the Naval Oceanographic Office (NAVOCEANO) were also used for comparison. Only the northern walls of ocean current features are considered in this study, which is broken into three main steps: Preprocessing, front extraction, and front comparison. First, RVL imagery is selected from Sentinel-1 ocean products, preprocessed to remove antenna mispointing artifacts, and all products from the same orbit are combined into a single swath. Second, front features are extracted from both the RVL and MURSST imagery using a ridge detection algorithm, the main ocean current is chosen from all ridge features using a ranking algorithm, and the northern wall of this current is extracted. Third, the RVL, SST, and in the case of the GS, NAVOCEANO GS locations, features are compared using a symmetric Hausdorff Distance (HD) measure, and Mean Hausdorff Distance (MHD). In some cases, the automatic front extraction failed by either misclassifying an eddy or similar ocean feature as the ocean current in either the RVL or SST image or failed to extract the entire length of the front visible within the image. All the SST and RVL fronts were classified manually to determine the success rate of the automatic front extraction and to exclude failed front extractions from the analysis, as they are not accurate representations of the SST and RVL data's ability to detect fronts. In special cases, the RVL image itself does not detect the entire ocean current, such that there are noticeable gaps in the ocean current. Similarly, in special cases the MURSST does not detect the entire ocean current. The automatic front extraction succeeded 65% of the time, including the special cases. The results demonstrated that RVL products were effective at determining the location of ocean fronts where the angle of the front's normal vector is within approximately 40° of the sensor's azimuthal heading. A mean HD of 31.9 km and a mean MHD of 13.2 km was calculated for all front pairs over all study areas. The RVL fronts appeared consistently to the north of the SST fronts, with an average offset of 25.4 km between the centroids of the SST and RVL fronts. Positive correlations were noted between cloud coverage and MURSST error in both study regions. Several RVL images detected ocean currents in regions of high MURSST error where the MURSST did not detect the ocean currents, suggesting that RVL may provide more accuracy than SST-based products in clouded regions where there is no auxiliary data.

Acknowledgements

First, I would like to thank Dr. Anders Knudby for his constant guidance, patience, and taking it in stride when almost everyone pronounces his name incorrectly. His insights are always pragmatic, sensible, and motivating. I have learned much concerning both the academic and wider world from this good-natured candor. I appreciate his kindness, sense of humour, and consideration for my future. I will be forever grateful for the day that he went out on a limb and agreed to supervise my undergraduate thesis, despite never having taught me before.

I would also like to thank my committee members Dr. Mike Sawada and Dr. Wesley Van Wychen, for their invaluable suggestions helping shape the final product you see today, as well as the myriad personal ways they have helped me. Many thanks to Dr. Wesley Van Wychen for exposing me to the concept of mapping ocean front features using radial velocity in the first place, as well as his extremely patient and encouraging guidance on the subject, and thanks to Dr. Mike Sawada for sparking my original interest in geomatics and encouraging my pivot to learning python, which forms the methodological bedrock for this thesis and has opened many new doors for me.

Thanks to all the wonderful Professors of the University of Ottawa Department of Geography, Environment and Geomatics, for their excellent and inspiring courses, and the great efforts they go to to help students like myself. I would also like to thank my friends for keeping me sane through the tumult of COVID and cancellation of my original thesis, as well as my labmates for their friendship, suggestions, and truly stimulating conversation when we probably should have been working. I have learned so much from each of them and shared many delicious snacks.

Finally, I would like to thank my family for their unyielding support, patience, and encouragement, not just for my thesis, but for all my endeavours. I am truly grateful to have met and learned from so many wonderful people, thank you all.

Table of Contents

List of Figures

List of Tables

List of Acronyms

AC	Agulhas Current
AMSR	Advanced Microwave Scanning Radiometer
ASF	Alaska Satellite Facility
AVHRR	Advanced very high-resolution radiometer
DAAC	Distributed Active Archive Center
ERDAAP	Environmental Research Division's Data Access Program
ESA	European Space Agency
GS	Gulf Stream
HD	Hausdorff Distance
IW	Interferometric Wide Swath Mode
LAADS	Level-1 and Atmosphere Archive & Distribution System
MHD	Mean Hausdorff Distance
MOC	Meridional Overturning Circulation
MODIS	Moderate Resolution Imaging Spectroradiometer
MURSST	Multi-scale Ultra-high Resolution Sea Surface Temperature Analysis
NAVOCEANO	Naval Oceanographic Office
NISAR	NASA-ISRO Synthetic Aperture Radar
NOAA	National Oceanic and Atmospheric Administration
OCN	Sentinel-1 Level-2 Ocean Product
PODAAC	Physical Oceanography Distributed Active Archive Center
RTOFS	Global Real-Time Ocean Forecast System
RVL	Radial Velocity
SAR	Synthetic Aperture Radar
SLC	Single-Look Complex
SST	Sea Surface Temperature

Chapter 1

Introduction

Currents span the world ocean in a great network, called the Meridional Overturning Circulation (MOC), transporting heat, water, biota, and nutrients in a continuous and directed manner. Their importance is paramount to life and the global climate system as we know it (Joseph, 2014). Great conveyors of heat, the MOC moves warm waters from the equatorial regions towards the poles, and cold waters from the poles towards the equators in a massive exchange of heat. The MOC also moves great volumes of water; for example the Antarctic Circumpolar Current that connects all of the global ocean basins, moves about 140 Sverdrups (Sv) of water, 1 Sv being one million cubic meters of water per second, in an important inter-basin exchange (Joseph, 2014). For comparison, all the world's rivers combined deliver about 1 Sv of freshwater to the ocean, and the world largest river, the Amazon, accounts for only about 0.2 Sv (Moura et al., 2016). The MOC also delivers about 10^{15} W of heat towards the poles, representing approximately a quarter of the total ocean-atmosphere heat circulation (Toggweiler, 2009). Surface ocean currents are apparent as hydrographic fronts, narrow regions with high temperature and salinity gradients separating two masses of water. Fronts are associated with elevated primary production as nutrients upwell from lower water layers towards the surface. Oceanic fronts have also been shown to have a significant effect on large scale atmospheric circulations, such as storm tracks (Joseph, 2014).

Detecting the boundary between warm surface ocean currents and the cooler surrounding water can be done using Sea Surface Temperature (SST) data, where it appears as a strong, observable gradient, also known as an SST front. SST data derived from satellite observations is effective for detecting ocean current fronts when conditions are favourable, i.e., cloud-free. However, cloud cover frequently obscures ocean currents in SST images. Ocean Radial Velocity (RVL) products are an alternative source of data that can be used to detect the fronts of major surface ocean currents without being impacted by cloud cover (Biron, Wychen, and Vachon 2018). Sea surface movement due to wave and current action imposed by SST gradients appears as a noticeable signature in RVL measurements, which represent the velocity component of the sea surface with respect to the sensor. As a result, RVL data can provide a proxy location for SST fronts (Van Wychen et al. 2018). Currently, fronts are typically detected directly using SST imagery, or using models that are based on SST data, shipboard temperature measurements, and temperature logging buoys, such as the Global Real-Time Ocean Forecast System. RVL data may help fill in gaps in these SST-based data sources during periods of persistent cloud cover. However, the accuracy with which fronts can be detected with RVL data is not fully

characterized and would benefit from better quantification to determine how to integrate RVL and SST products optimally.

This thesis investigates how effectively RVL imagery can predict the position of ocean currents compared to contemporary SST-derived methods using two case studies: the Gulf Stream (GS) and the Agulhas Current (AC). It expands upon the current literature by better quantifying the accuracy of RVL-derived fronts under varying conditions compared to SST-based methods. To this end, RVL imagery will be used to detect the location of the northern walls of the Gulf Stream and the Agulhas Current, over the course of 2020. The relative accuracy of these detections will be quantified by comparison to ocean current locations derived from a global model of daily SST. In the case of the GS, a Naval Oceanographic Office (NAVO) operational front product derived from the Global Real-Time Ocean Forecast System (RTOFS) will also be used in the comparison. Cloud masks will help determine the possible influence of cloud cover on the difference in ocean front locations estimated by the three different products.

1.1 Thesis Format

This thesis is written in an article format, so some of the information in the thesis introduction and conclusion is reiterated within the article below. The following chapter represents the article and basis of this thesis. The article's overall structure is based on the guidelines for submission to the International Journal of Remote Sensing.

Chapter 2

An automated approach to mapping ocean front features using Sentinel-1 with examples from the Gulf Stream and Agulhas Current

Andrew Newall [a], Anders Knudby [a], Wesley Van Wychen [a, b]

[a] *Department of Geography, Environment and Geomatics, University of Ottawa, Ottawa, Canada;* [b] *Department of Geography and Environmental Management, University of Waterloo, Waterloo, Canada*

Abstract

This study assessed the ability of Sentinel-1 radial velocity (RVL) products to mark the position of ocean current front features over the course of a year, using the Gulf Stream (GS) and Agulhas Current (AC) as case studies. RVL-derived front features were compared against fronts derived from Multi-scale Ultra-high Resolution Sea Surface Temperature Analysis (MURSST) data. In the case of the Gulf Stream, both the RVL and SST derived fronts were also compared to a Naval Oceanographic Office (NAVO) operational front product derived from the Global Real-Time Ocean Forecast System (RTOFS). A ridge filter was used to find fronts in both the SST and RVL data, and the similarity between each pair of fronts were measured using the discrete Hausdorff distance (HD) and Mean Hausdorff Distance (MHD). In some cases, the automatic front extraction failed by either misclassifying an eddy or similar ocean feature as the ocean current in either the RVL or SST image or failed to extract the entire length of the front visible within the image. SST and RVL fronts were classified manually to determine the success rate of the automatic front extraction and to exclude these inaccurate front extractions from the analysis. The results demonstrated that RVL products were effective at determining the location of ocean fronts where the angle of the front's normal vector is within approximately 40° of the sensor's azimuthal heading. A mean HD of 31.9 km and a mean MHD of 13.2 km was calculated for all front pairs over both study areas. The RVL fronts appeared consistently to the north of the SST fronts, with an average offset of 25.4 km between the centroids of the SST and RVL fronts. Positive correlations were noted between cloud coverage and MURSST error in both study regions. In addition, several RVL images detected ocean currents in regions of high MURSST error where the MURSST did not detect the ocean currents, suggesting that RVL

may provide more accuracy than SST-based products in clouded regions where there is no auxiliary data.

1. Introduction

Detecting the boundary between warm, fast-flowing ocean currents and the cooler surrounding water can be done using Sea Surface Temperature (SST) data, where it appears as a strong, observable gradient, also known as an SST front. SST data derived from satellite observations are effective for detecting ocean fronts when conditions are favourable, i.e., cloud-free. However, cloud cover frequently obscures ocean currents in SST images. For example, a mean annual cloud cover of 70% obscures the Gulf Stream (GS) region (Kuang et al. 2012) and between 50-100% depending on the area for the Agulhas Current (AC) region (Lutjeharms, 1981). Sentinel-1 Ocean Radial Velocity (RVL) products are an alternative source of data that can be used to detect the fronts of major surface ocean currents such as the GS and AC regardless of cloud cover (Biron et al., 2018). Sea surface movement due to wave action imposed by wind, current shear, and convergence zones appears as a noticeable signature in RVL data (Chapron et al., 2005), which measure the velocity component of the sea surface towards or away from the sensor. As a result, RVL data can provide a proxy location for SST fronts (Van Wychen et al., 2018). Currently, front positions are often estimated using oceanographic models (Van Wychen et al., 2018). These models, such as the Global Real-Time Ocean Forecast System, are based on SST data, shipboard temperature measurements, temperature logging buoys and other auxiliary data. RVL data may help fill in gaps in these models during periods of persistent cloud cover. However, the accuracy with which fronts can be detected with RVL data is not fully characterized and would benefit from better quantification to determine how to integrate RVL and SST products optimally.

This study aimed to determine the effectiveness of RVL data at detecting the position of ocean front features by automatically extracting front positions from RVL data and a contemporary global SST model, the MURSST. The fronts successfully extracted from both datasets were then compared using Hausdorff Similarity measures. Gulf Stream front positions from NOAA were used as an additional product in the comparison for the Gulf Stream region. Cloud masks were used to help determine the relationship between cloud cover and the MURSST error.

1.1. Study Areas

GULF STREAM

The GS is a warm, fast flowing ocean current that originates in the Gulf of Mexico, follows the coast of the United States until Cape Hatteras, North Carolina (Chassignet & Garraffo, 2001), and then dissipates as it crosses the Atlantic

Ocean. The GS moves in a meander with a wavelength approximately between 200 km and 400 km, with amplitudes of the wave generally increasing eastward, except in the summer when very large amplitudes occur as complicated thermal conditions arise (D. V. Hansen, 1970). The strength and position of the GS influences many important systems: the local climate of the east coast of North America and the west coast of Europe (Lambhate et al., 2021), the formation of clouds and cyclones (Minobe et al., 2008), the productivity of ecosystems and commercial fisheries (Zhang & Gawarkiewicz, 2015), the detection of submarines (Peloquin, 1992), and the optimal location of global shipping routes (Joseph, 2014; Lo & McCord, 1995). The total water transport of the GS ranges over time and space, with an average of around 30 million cubic meters per second (30 Sverdrup; Sv) near Florida to around 150 Sv near Newfoundland (Bower & Hogg, 1996). The bounds of the Gulf Stream considered in this study are 30°N to 43°N, and 80°W to 60°W (Figure 1).

AGULHAS CURRENT

The Agulhas Current is the strongest western boundary current in the Southern Hemisphere, transporting about 65 Sv (Lutjeharms, 2006). It flows southwards along the coast of Southern East Africa from 27°S, into the open ocean south of South Africa, where it retroflects backwards (Figure 1Error! Reference source not found.; at about 19°E) and flows eastwards due to shear interactions with the eastward running Antarctic Circumpolar Current, leaking water into the South Atlantic in the forms of filaments and rings, and transferring large amounts of heat and salt with them (Lutjeharms, 2006). This leakage has significant climatic effects and is an important source of heat for the South Atlantic. It is also known to affect rainfall over South Africa, coastal weather, marine biota and nutrient distribution (Lutjeharms, 2006). The bounds of the AC used for this study are from 30°S to 42°S, and from 27°E to 10°E (Figure 1), slightly larger than the region given by Gordon (1985) for where it separates from the African continent.

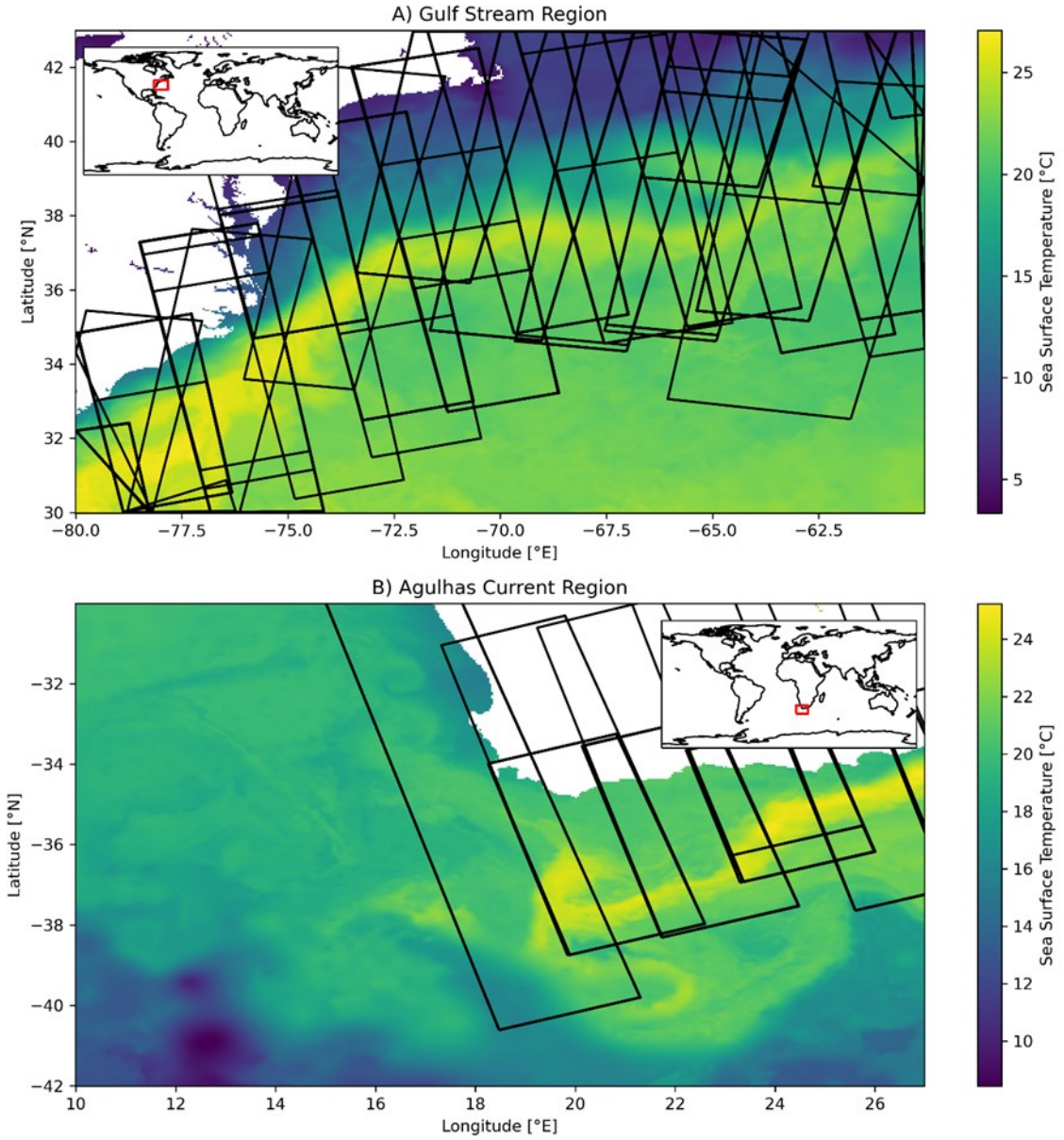

Figure 1. A) The Gulf Stream study area bounds, and B) Agulhas Current study area bounds. Both figures show the MURSST for 2020-01-01 and show the study area bounds in red on the inset global maps, with all the RVL swath boundaries for both study areas overlaying the MURSST in black.

2. Materials and Methods

2.1. Data Overview

We used Copernicus Sentinel-1 RVL data processed by the European Space Agency (ESA) and retrieved from the Alaska Satellite Facility Distributed Active Archive Center (ASF DAAC) (ESA, 2020), the dates for RVL products within the study area are listed in Table 4. We also used the MODIS35 L2 Daily Cloud Mask (Ackerman & Frey, 2015), Multi-scale Ultra-high Resolution Sea Surface Temperature Analyses (MURSST) data from the Physical Oceanography Distributed Active Archive Center (PODAAC) (NASA/JPL, 2015), and data from the Global Real-Time Ocean Forecast System. GS locations from the Naval Oceanographic Office (NAVOCEANO) were obtained courtesy of Todd Spindler (todd.spindler@noaa.gov) and Robert Daniels (robert.daniels@noaa.gov) of the National Oceanic and Atmospheric Administration (NOAA).

2.2. Data Background

The RVL product is derived from Sentinel-1 Level 1 Single-Look Complex (SLC) Synthetic Aperture Radar (SAR) data taken in Interferometric Wide (IW) swath mode. It is calculated by observing a shift in Doppler frequency between the observed Doppler, and the predicted Doppler, which is a predicted signal based on the estimated motion of the sensor and the Earth, resulting in a phase shift if the target has moved relative to the antenna. This "Doppler Anomaly" can be used to determine the radial velocity of surface displacement relative to the sensor. Rather than a direct surface current measurement, the radial velocity of the ocean surface is the line-of-sight velocity; that is, the component of the ocean surface's velocity moving towards or away from the radar source (Chapron et al., 2005; Johannessen et al., 2008; Engen & Johnsen, 2015; Figure 2).

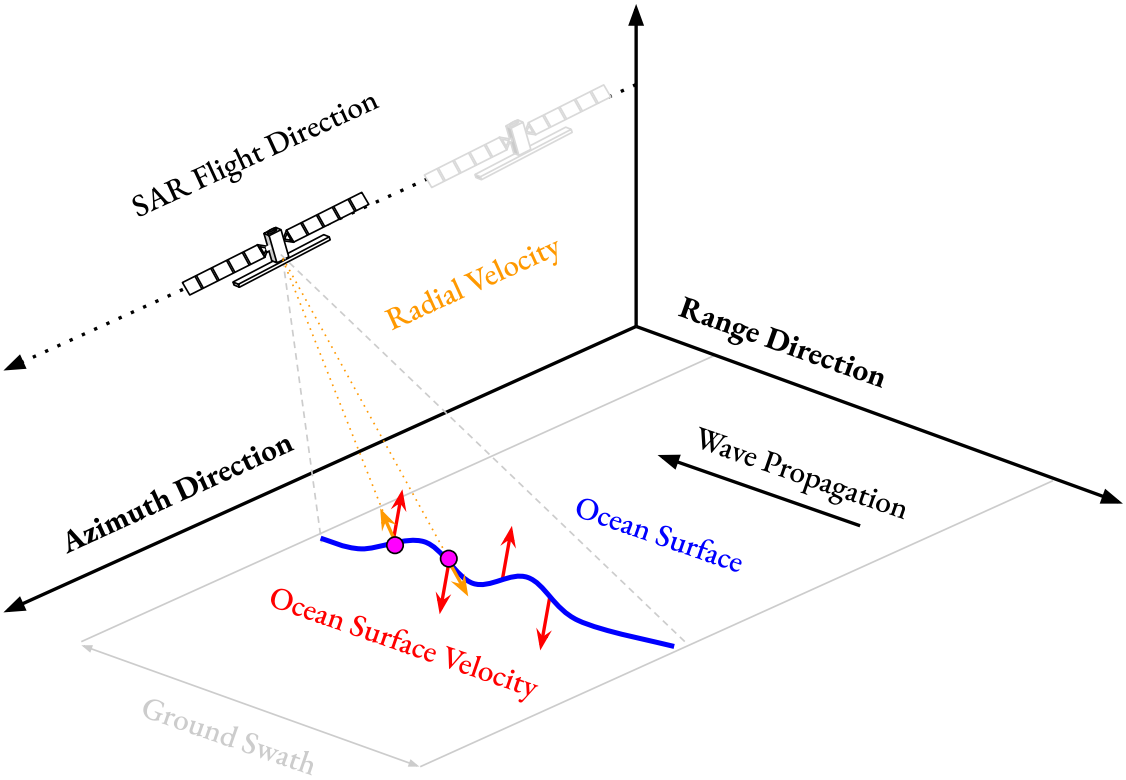

Figure 2. Diagram depicting radial velocity measurements over the ocean. Example shows two facets (purple) on a propagating wave, the surface velocity of those facets (red) and the radial velocity component of the surface velocity at those points (orange).

This velocity is positive when moving away from the radar antenna, and negative when moving towards it. The Doppler shift results from movement of the sea surface, which is dependant on many factors, such as the combined action of near surface wind, wave breaking, and surface current. Steep ocean swells and waves produce noticeable signatures in RVL data, where there are high velocities towards or away from the satellite, relative to the surrounding calmer ocean (M. W. Hansen et al., 2011). A water mass boundary, such as the fronts on either side of a warm current flowing through colder waters, can produce noticeable gradients in RVL images where greater horizontal ocean surface wind speeds on the warm side of the front increase wave action and surface roughness relative to the cold side (Jones et al., 2012). This allows the RVL to act as a proxy for detecting SST front locations. However, the raw Sentinel-1 RVL products suffer from an error based on imperfect satellite position estimation, which introduces error in the Predicted Doppler and consequently creates noticeable scalloping artifacts (Danilo and Bella 2018; Figure 4). These must be compensated for with a smoothing step.

MURSST is a global daily SST estimate based on the fusion of two infrared sensors (the Moderate Resolution Imaging Spectroradiometer (MODIS) and the Advanced very high-resolution radiometer (AVHRR)), several microwave sensors (the Advanced Microwave Scanning Radiometer (AMSR-E), Advanced Microwave Scanning Radiometer 2 (AMSR2), and Windsat), and in-situ

measurements from iQuam (Chin et al., 2017). An estimation of the standard deviation of error is included in the product, given in degrees Celsius.

The MODIS35 L2 Daily Cloud Mask is based on MODIS Aqua retrievals. Note that between August 16th and September 2nd 2020, Aqua MODIS suffered a science data outage, and the products are completely missing from the MODIS cloud mask record over the Agulhas Current region due to this outage (NASA, 2020).

The NAVOCEANO Global RTOFS Gulf Stream locations are generated from the intersection of the 12°C isotherm and the 400m isobath in the RTOFS ocean model, which is closely related to The Hybrid Coordinate Ocean Model (HyCOM).

2.3. Methods Overview

Data processing followed three steps (Figure 3), each of which are explained in more detail below:

1. RVL rasters were preprocessed by applying a smoothing and filtering to each scene, then combining all RVL scenes from the same orbit and day into a single composite swath image.
2. The northern walls of the ocean fronts were extracted from the resulting daily RVL composites, as well as from the MURSST daily rasters.
3. The fronts derived from RVL data, SST data, and the NAVOCEANO fronts in the case of the GS, were compared to each other using the Hausdorff distance (HD) function, which quantifies the greatest discrepancy between two fronts (Eiter & Mannila, 1994; Huttenlocher et al., 1993a), as well as the Mean Hausdorff Distance (MHD), which quantifies the average discrepancy between two fronts. The distance between the centroids of each front in the comparison were calculated. The MODIS cloud mask was used as auxiliary data to determine what proportion of the detected fronts are under cloud cover. Additional data was collected during the front comparison, such as the temperature range of the scene, the mean annual cloud coverage of the scene, data relating to the offsets between the centroids of each front pair, and data relating to anomalous gaps in the ocean currents that sometimes occurred in the RVL and SST images.
4. Front pairs were manually classified when an automatic front extraction failed by misclassifying the ocean current or by failing to extract the entire front visible in either image. Special cases where the RVL or MURSST data had the anomalous gap over part of the ocean current were classified separately.

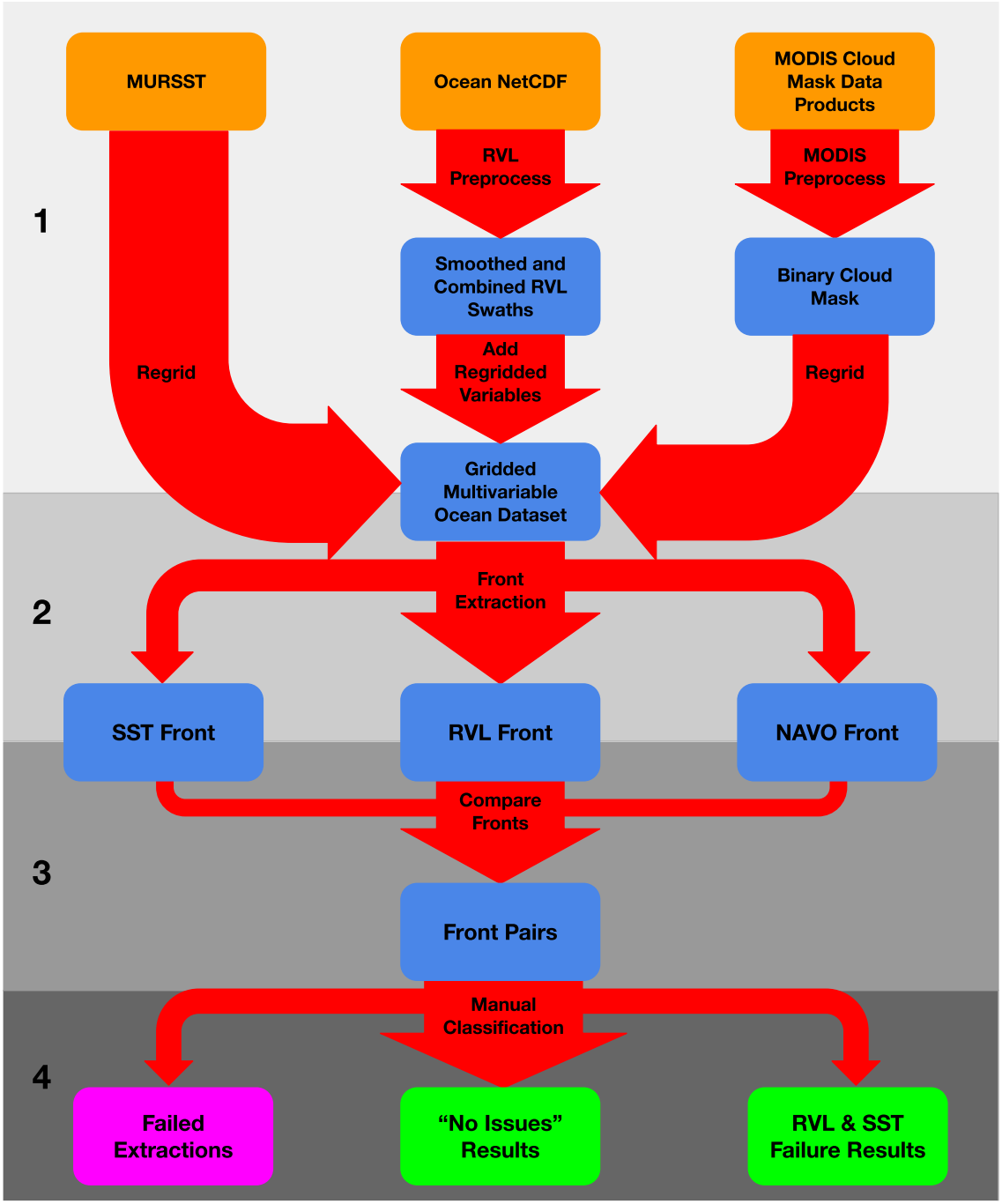

Figure 3. Overview flowchart of methods. Orange boxes indicate inputs, blue intermediate products, purple the failed extractions, and green the results.

2.4 Preprocessing

2.4.1. Radial Velocity Preprocessing

The RVL data were obtained in the form of zipped Sentinel-1 Level-2 Ocean (OCN) product NetCDF files that contain the surface radial velocity data, among other SAR-derived layers. The RVL data itself is composed of three subswaths per product, stacked in the range direction with some overlap between subswaths. The RVL data was filtered and smoothed using a modified version of Danilo and

Bella's method (2018) to reduce a strong signal processing signature inherent in the data (Figure 4A). An important part of their method is to use land as a reference point within RVL subswaths to determine bias, because land should have a radial velocity of zero. However, most RVL images of the study area contain no land, so it cannot be exploited to determine the bias in the RVL. Instead, the swaths were filtered for biased points, then detrended along their range and then azimuthal directions, providing an improved signal but inaccurate RVL values. First, cells in the raw subswaths (Figure 4A) with geophysical doppler standard deviation values above 4.0 were removed (Figure 4B); this value was determined empirically by Danilo and Bella (2018). The mean of the entire swath in the range direction was then calculated and used to filter out the steep drops at the borders of the subswaths, slope values beyond 1.0 were removed (Figure 4C); the mean profile in the range direction was never found to approach these values aside from the steep drops at the borders. The filtered swaths were then detrended in the range direction using a Savitzky-Golay (SG) filter (Figure 4D). The SG filter fits a variable order polynomial over a variable sized window, using least squares fitting. An advantage of SG filters is their ability to reduce noise while maintaining the height and shape of the waveform (Schafer, 2011). A third-order polynomial over a window size of 51 was used for filtering; these values were selected as they provided the smoothest results, free from noticeable scalloping artifacts, as determined by visual interpretation during experimentation, and a third order polynomial fit was implemented by Chapron et al. (2005). The range detrended swaths were then used to calculate the mean in the azimuthal direction. The swaths were detrended again, this time along the azimuthal direction, again using the SG filter (Figure 4E).

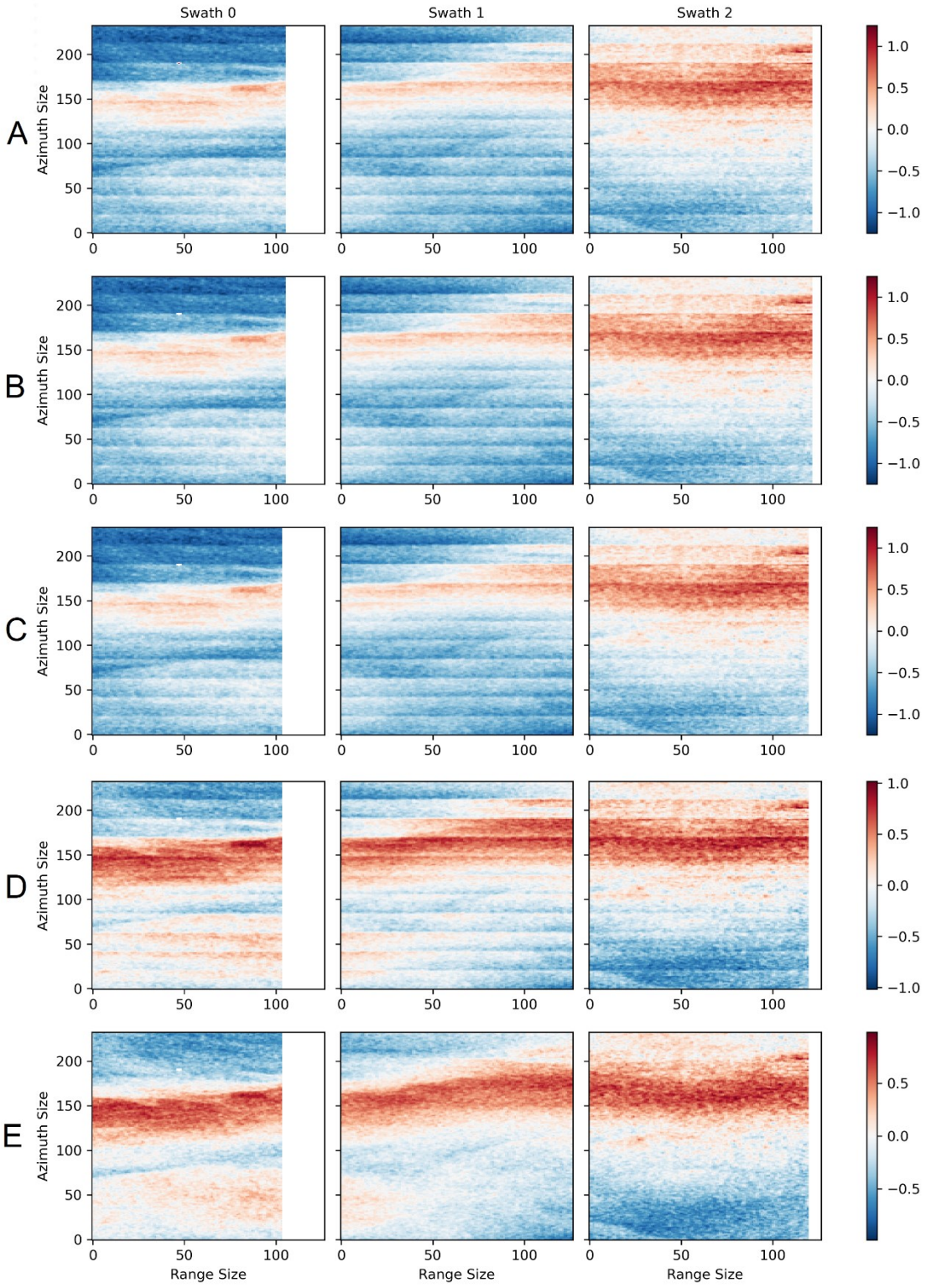

Figure 4. Comparison of raw radial velocity data to smoothed radial velocity data for January 7, 2020. A) Raw RVL image, B) RVL with doppler standard deviation values above 4.0 removed C) The filtering of steep borders of each subswath; steep borders are not highly visible since they make up a small proportion of pixels at the rightmost edge of each subswath. D) Swath detrended with SG in range direction. E) Swath detrended in the azimuthal direction. All images are radial velocity in meters per second. Note value ranges change for E) to maintain visibility of the signal.

Once smoothed, all subswaths were converted into an array of points with their RVL values, land mask values, and the latitude/longitude coordinates of the cell centers. These arrays were reprojected from their 1km x 1km cell swath with geodesic coordinates at their cell centers to a 0.009 decimal degree resolution WGS84 projection using a nearest neighbors resampling (0.009 degrees closely approximates the 1km resolution of the RVL product in the latitudinal direction). Swaths were assumed to be continuous in the azimuthal direction, so the first and third subswaths were adjusted to match the mean value of the central swath in the overlapping regions. If land was present in the combined RVL, the image was adjusted such that the average radial velocity over land was zero by subtracting the average radial velocity of land cells from the entire image. This step was applied to provide more nominally accurate RVL values, as the signal itself is not changed and it has no effect on the front extraction. The reprojection allowed for the combination of swath scenes of the same day and orbit, in the reference frame also used by the MURSST and MODIS cloud mask data. The MURSST and MODIS data were then resampled to the same grid as the RVL image using nearest neighbour resampling. Swaths from the same day and orbit were similarly combined in an array and nearest neighbor resampled to a larger grid of the same resolution.

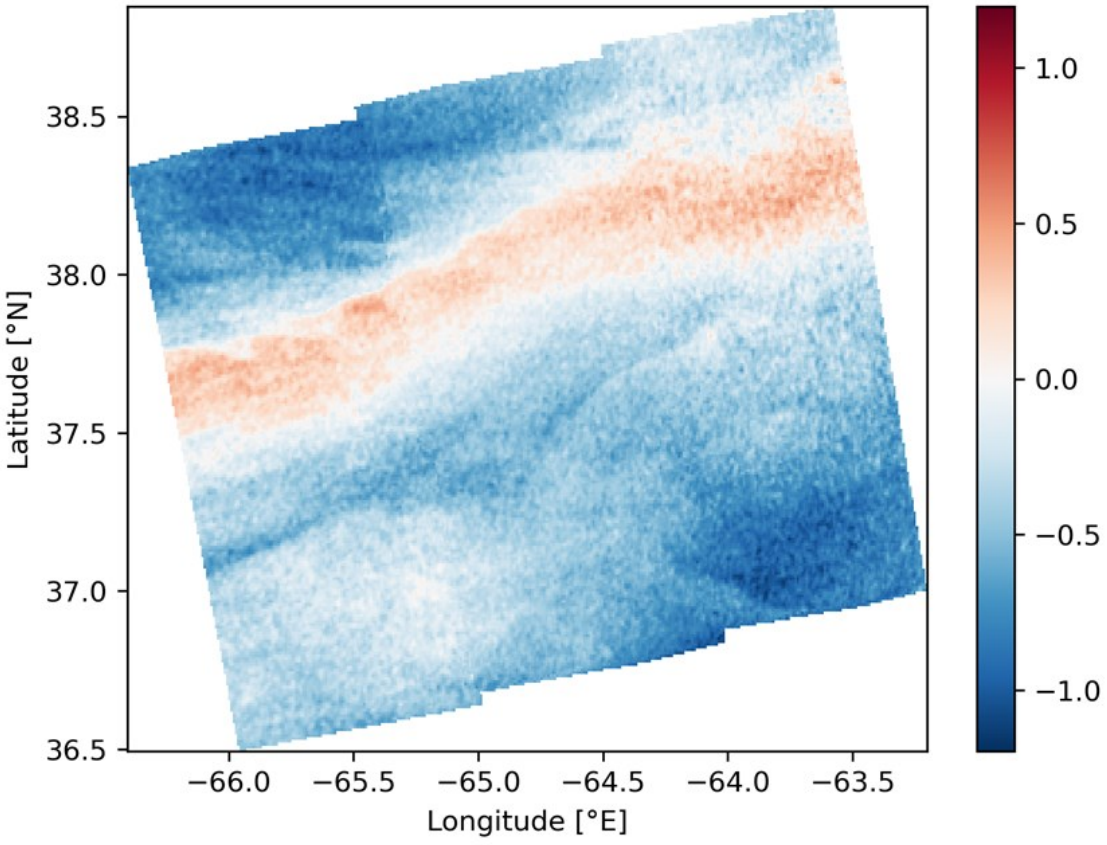

Figure 5. Reprojected RVL swaths for January 7, 2020.

MODIS Cloud Mask Preprocessing

The MODIS cloud masks were obtained as a collection of GeoTIFFs. Bit 0 of the 8-bit GeoTIFF contains the bitflag representing whether a cloud quality flag was determined (1) or not determined (0), while undetermined cells appear as null values in the output binary mask. Bits 1 and 2 contain the cloud presence bitflags: 00 is "cloudy", 01 is "uncertain clear", 10 is "probably clear", and 11 is "confident clear". A binary cloud mask for each day was created by grouping 00 and 01 to represent "cloudy", with 10 and 11 grouped to represent "clear", as suggested by Strabala (2005).

2.5 Front Detection

Detecting the ocean fronts in the pre-processed RVL data involved a sequence of steps. First, both SST and RVL images were smoothed using a gaussian filter to focus on features the scale of the ocean current. Without a smoothing, image noise causes the existence of many smaller, disparate pieces of the front to be extracted as there are many large temperature and RVL gradients at scales much smaller than the ocean current's large-scale temperature gradient. A sigma of 50 was chosen as it approximates the general width of an ocean current feature in the given study areas, 50km. Next, ocean features (e.g., the AC, GS, and eddies) were detected using a ridge finding algorithm, and an 80^{th} percentile threshold was applied to the ridge filtered images to segment the images into ocean features. The properties of each feature were then ranked by a linear algorithm to select the feature most likely representing the ocean current. The northern wall of this feature was extracted as the front. Each of these steps is outlined in greater detail below.

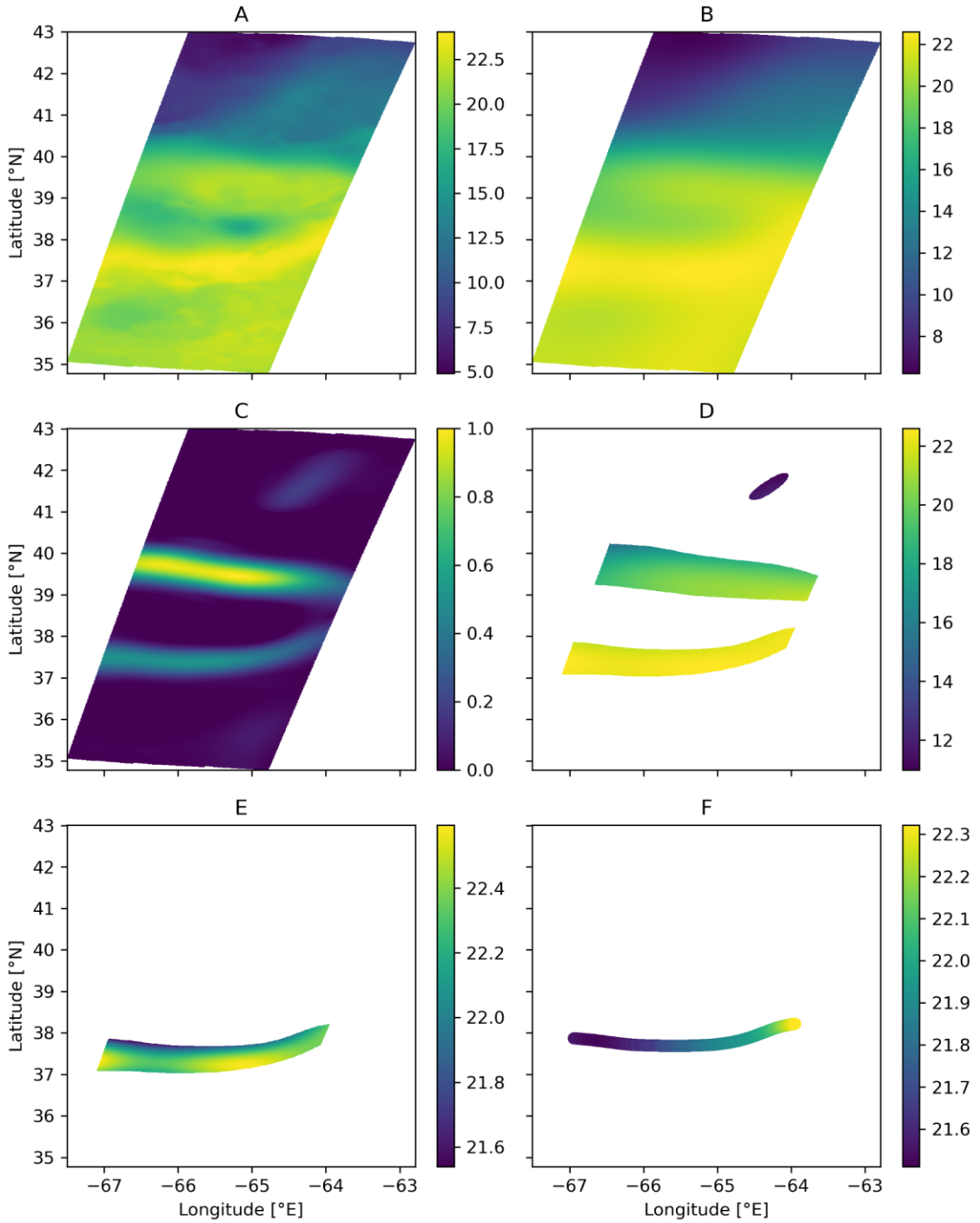

Figure 6. Ocean current front extraction workflow example. SST image for 2020-01-01 in the GS region. A) SST with the same gridding and extent as the RVL swath. B) Gaussian smoothed SST (sigma=50). C) Ridge filtered SST, values are a unitless 'ridge' measure between zero and one. D) SST where the ridge filtered image is greater than its 80th percentile, represents ocean features. E) The ocean feature selected using the linear algorithm based on which feature has the properties most likely belonging to an ocean current. F) The northern wall of the selected feature (plotted as enlarged points for visibility). All images except C are in degrees Celsius, note that the colour bar scales change between images to maintain visibility of the signals.

Ridge Filter

Front features were detected using the Multiscale vessel enhancement filtering (Frangi et al. 1998). This algorithm examines the second order local partial derivatives of the images to find regions of high local curvature. Within SST and RVL imagery, front features appear as such regions of high local curvature due to the relatively rapid transition between the warm water of the current and the cooler surrounding water, and the relatively rapid transition between the higher wave action on the warm side of the current's front and the reduced wave action of the surrounding cooler waters. The filtered image is thresholded to values above 80^{th} percentile, a value determined through visual analysis to provide the best results. This segmented image contains one or more features, representing ocean features of all kinds, such as rings and eddies, as well as ocean currents.

A manual classification of a random sample of segmented images was performed, classifying every segmented feature within each image as either ocean current, or non-ocean current. A large list of properties was calculated for each feature (e.g., mean value, area, eccentricity, minimum value, maximum value, etc.). A logistic regression was performed using the classified data to determine the most important predictors for distinguishing the ocean currents from other ocean features (i.e., the properties with the highest feature importance in the linear regression model). The most predictive properties were determined to be the max value (SST or RVL, depending on the input image), 90^{th} percentile value, mean value, area, and solidity (area divided by the area of the feature's convex hull). These properties were standardized by subtracting the mean and scaling them to unit variance (a standard scaling). The sum of all the scaled properties formed a ranking value for each feature. The highest ranked feature in each image was determined to be the ocean current. For example, Figure 6C shows the output of the ridge filter, where the eddy above the ocean current is a noticeable feature because it also represents a region of high local curvature. However, in Figure 6D it becomes apparent that the feature representing the ocean current (Figure 6E) is hotter than the eddy, demonstrating its use as a distinguishing variable. This temperature property, along with the aforementioned properties, allows the algorithm to estimate the feature most likely representing the ocean current, i.e., the feature with the highest rank.

The medial axis of the chosen feature bisects the feature in two along its longest axis. This was used to approximate the core of the ocean current feature, with the border of the feature representing its walls, i.e., the northern and southern ocean current fronts. By excluding any ocean current front values south of the core, only the northern wall ocean current front feature remained, representing the final front feature used in this study. The values at the center of the cells for the feature were then output as multipoint shapefiles, in preparation for final analysis.

2.6 Front Similarity Analysis

Similarity Measures Overview

To quantify the accuracy with which ocean fronts can be detected in the RVL data, the locations of the mapped RVL fronts were compared to the corresponding locations of fronts derived from the MURSST data and NAVOCEANO data. While simple proximity measures such as Euclidean or geodesic distance exist to quantify the difference in location between the two sets of points, most do not suffice to measure their overall similarity in terms of shape and location. The difficulty in quantifying the similarity of the point sets (in this case, ocean fronts in the form of multipoint shapefiles) using simple distance measures is that they may not only be offset translationally, but may also differ in length, shape, and orientation. Figure 7 shows examples of the differences between point sets that affect their similarity. The Hausdorff Distance metric is sensitive to all these differences.

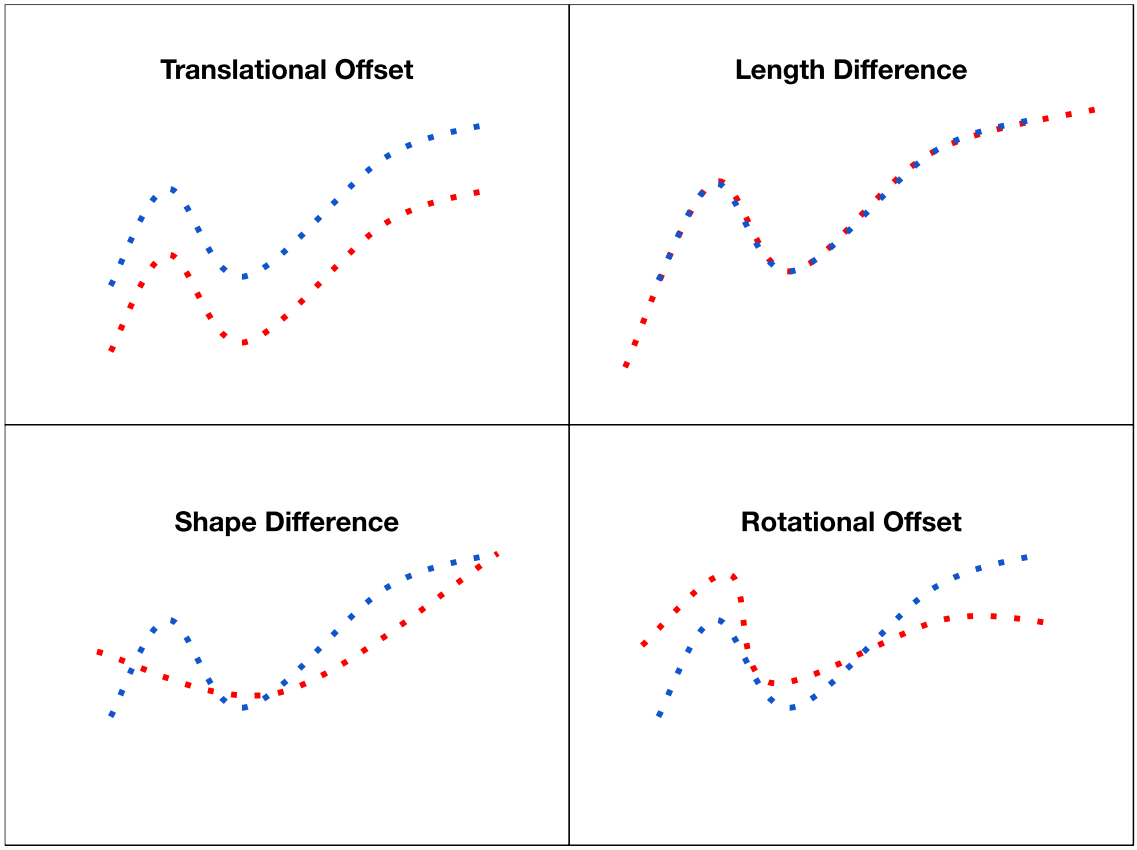

Figure 7. Factors between two point-sets that affect similarity.

Hausdorff Distance

The oriented Hausdorff Distance measures the greatest discrepancy between two sets of points; for every point in the first set, the distance to the closest point in the second set is measured, and the Hausdorff Distance is calculated as the largest of these point-pair distances. However, this is a directional measure; the distance

from the first set of points to the second is not necessarily equal to the distance from the second set to the first. To avoid this problem, the "non-oriented" Hausdorff Distance computes the oriented Hausdorff Distance in both directions and selects the larger of the two (Huttenlocher et al., 1993b). The non-oriented Hausdorff Distance (henceforth: HD) was used here to quantify the difference between ocean current fronts detected with RVL data, MURSST data, and the NAVOCEANO GS front product. Because this metric determines the greatest deviation between the two curves being examined, it is very sensitive to discrepancies in shape and length, and thus serves as a measure of shape similarity in addition to positional difference (Min et al., 2007). Because of this, it is also very sensitive to outliers. Hausdorff Distance measures are most often used in computer vision applications (Huttenlocher et al., 1993b), but have also previously been applied to SST fronts (Lambhate et al., 2021).

Mean Hausdorff Distance

The Mean Hausdorff Distance takes all the minimum point-pair distances as is done for the oriented Hausdorff distance, but rather than selecting the largest as the result, it averages all of them. This average is taken in both directions, as per the non-oriented Hausdorff Distance, and the mean of these two values represents the final Mean Hausdorff Distance (MHD). Rather than the greatest discrepancy between two point-sets measured by the HD, the MHD represents the average discrepancy, so it is less sensitive to outliers and differences in length.

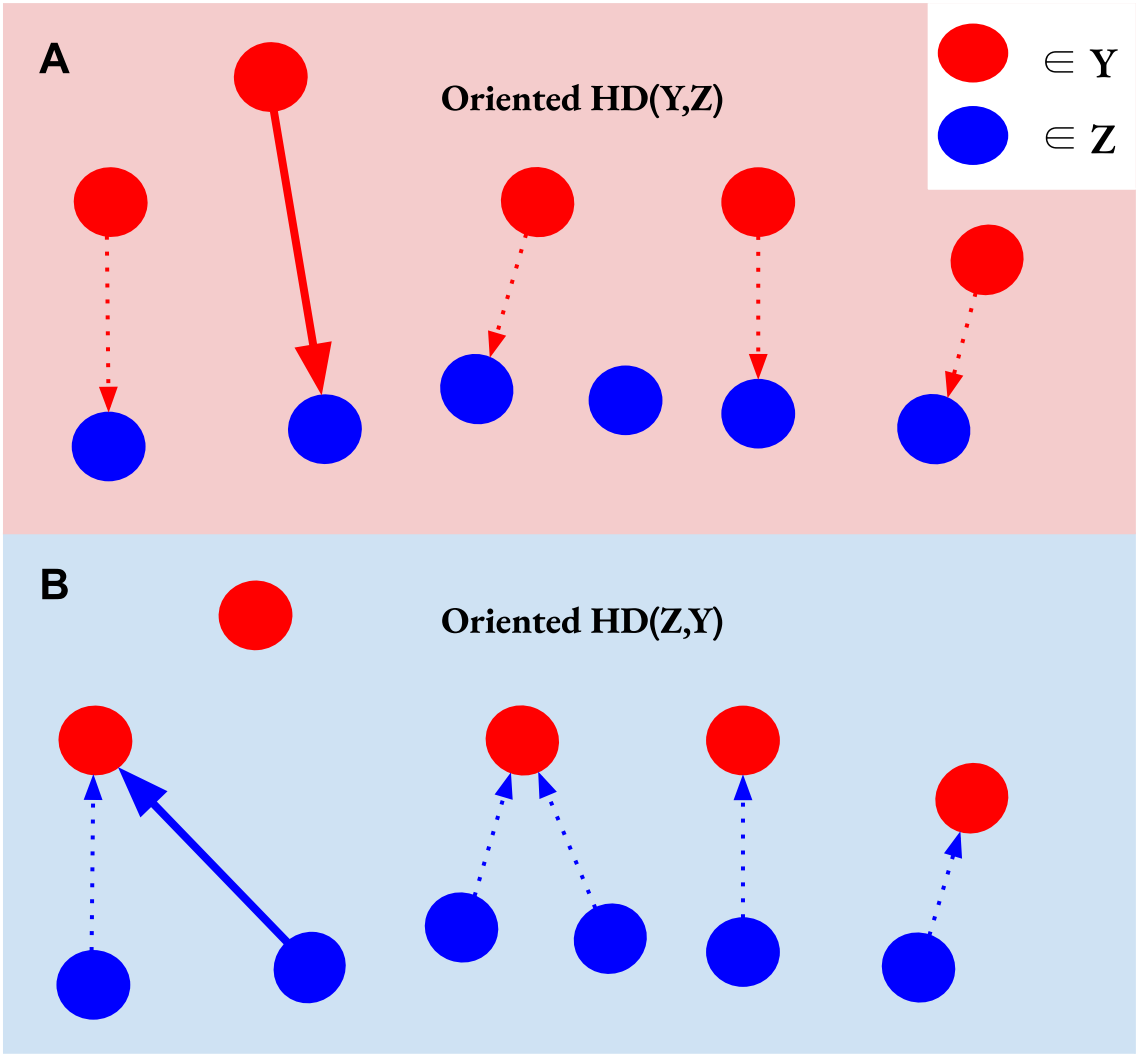

Figure 8. Example of oriented Hausdorff distance calculated between two point-sets, set Y (red) and set Z (blue). First, the Hausdorff distance is calculated from set Y to Z (A), then Z to Y (B). The dotted arrows represent the distance to the nearest point in the opposite set (i.e., the minimum distance). The solid arrows represent the largest of these minimum distances, i.e., the oriented Hausdorff distance. Note that HD(Y,Z) is not equal to HD(Z,Y); the non-oriented Hausdorff distance is the larger of these two. The Mean Hausdorff distance is the average length of all the arrows. Modified from Bulbul et al. (2011).

2.7 Analysis

Once the RVL and SST fronts were obtained, the HD and MHD were calculated between RVL and SST fronts for every available daily orbit, and between the NAVOCEANO fronts and the RVL and SST fronts for the GS. In addition, the following data were also calculated during the comparison: the offset distance and compass heading direction between the centroids of each front pair, the temperature range of the scene, average annual cloud coverage within the scene (Figure 9), daily percentage of cloud over the fronts, and the average MURSST error over the fronts were calculated for each swath, and in cases where the SST and RVL intersected, the normal angle of the SST front feature at that

intersection point. This last value was used to determine the "RVL failure angle" discussed in the following sections.

The results were examined visually to determine whether the swath contained the ocean current in question, and those that did not were discarded. Of the swaths that contained the ocean current, some were cases where the feature selection algorithm failed to classify the correct ocean feature, or the ridge filter only partially extracted one or both fronts. These misclassifications (where the wrong feature was identified as the ocean current), as well as partial classifications (where the ridge filter did not identify the whole feature), their modes of failure, and how they were identified, are discussed in more detail in the following section. The misclassified and partially classified swaths are excluded from the results, as they fail to provide an accurate set of the ocean current front positions within the swath for comparison.

Of the front extractions where the extraction algorithm correctly classified the ocean current in both images and extracted the entire visible front, there were a small proportion of cases where the ocean current has no signal in part of the RVL image, as well as a small proportion of cases where the MURSST image itself fails to detect part of the ocean current within the swath. Instead, a gap in the ocean current is seen. Both cases were specially classified, and they are considered independently at the end of the results.

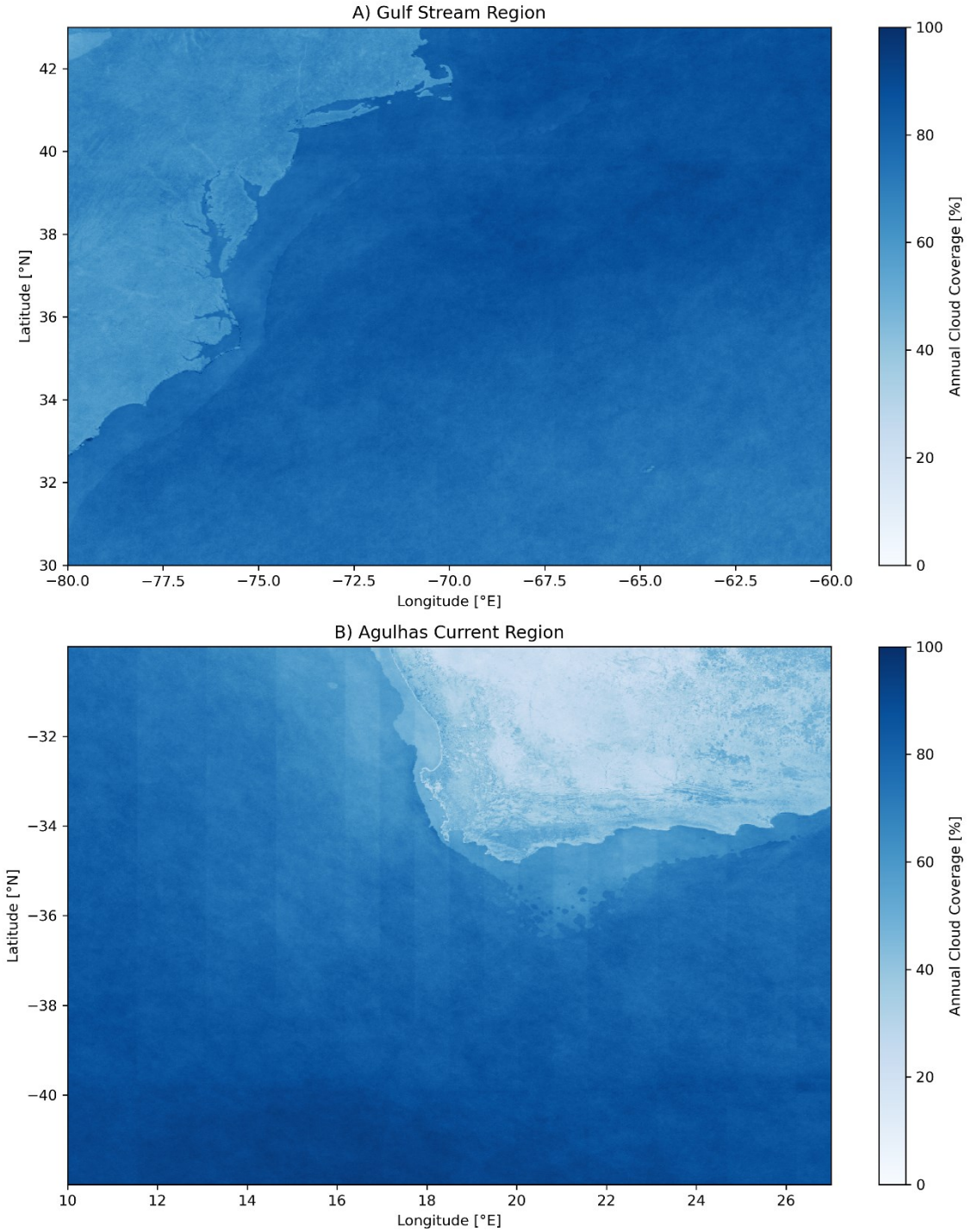

Figure 9. A) Percentage of annual cloud coverage in the Gulf Stream and B) Agulhas Current study regions for 2020. Note that annual cloud coverage is generally higher in the vicinity of the ocean currents.

Classification Process

A number of issues affected swaths for both study areas, and prior to calculation of summary statistics a manual classification of swaths was conducted to exclude problematic swaths from further analysis and separate special cases for separate analysis.

All fronts were output with plots of the SST within the swath region, the RVL swath, the RVL and SST fronts, and a map showing the location of the swath in the study region (like the rows in Figure 10 and Figure 11). These visuals were used during the manual classification of the front pairs. Swaths that have been misclassified due to the failure of the front extraction process rather than the data itself failing to detect the ocean current feature do not provide an accurate assessment of the RVL's efficacy at portraying the location of the fronts. For this reason, they were identified manually and excluded from the analysis. During this process, other special cases were also classified. The classification included the following classes:

1. "Out of bounds": the swath contains no ocean current and is excluded from analysis (Figure 10A).
2. The methods extract fronts as intended, but the RVL data itself fails to detect the ocean current apparent in the SST data (Figure 10B). These swaths are considered separately in the results.
3. The methods extract fronts as intended, but the SST data fails to detect the ocean current apparent in the RVL data (Figure 10C). These swaths are considered separately in the results.
4. Swaths where either the SST or RVL were misclassified due to a failure of the feature selection algorithm (e.g., by selecting an eddy rather than the ocean current), but appear clearly within the image, were considered misclassified (Figure 11D). These swaths were excluded from the analysis.
5. Swaths where either the RVL or SST was only partially identified by the ridge detection algorithm, but a human could reasonably be expected to classify the front were considered partial extractions (Figure 11E). These swaths were excluded from the analysis.
6. Swaths where both the RVL and SST fronts were classified correctly and where the fronts were completely extracted were considered to have "No Issues" (Figure 11F). These swaths were used to calculate the summary statistics, time series, and correlations for both study areas.

Examples of each classification are shown in Figure 10 and Figure 11.

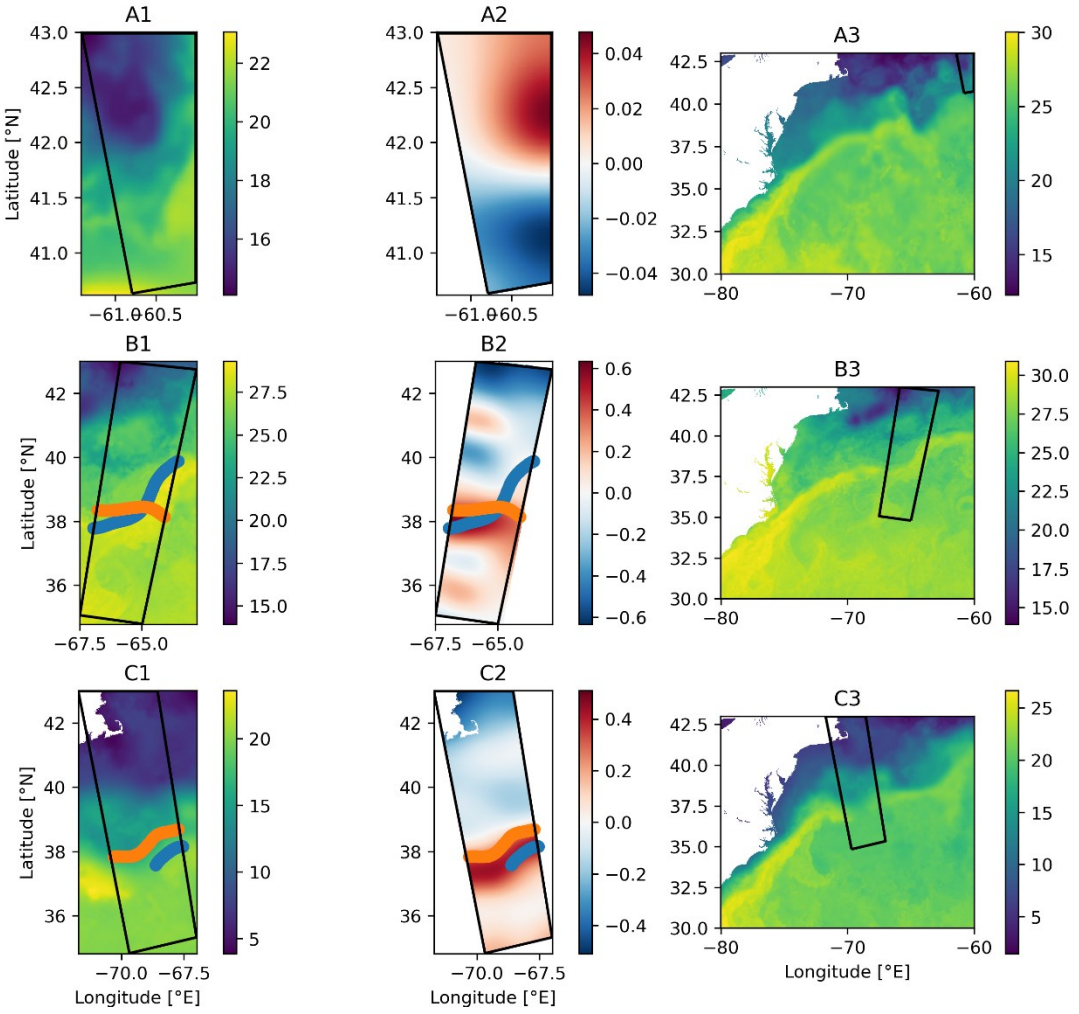

Figure 10. Examples of problematic swaths from the GS study area. Column 1 shows the MURSST within the swath's bounding box (°C), column 2 shows the RVL data (m/s), column 3 shows the MURSST over the whole study area (°C), with the black box indicating the location of the RVL swath. Orange lines represent the RVL front, blue lines represent the SST front. A) Swath does not cover the GS north wall, which is located outside the swath to the south. B) RVL fails to detect the entire ocean current. C) MURSST fails to detect the entire ocean current.

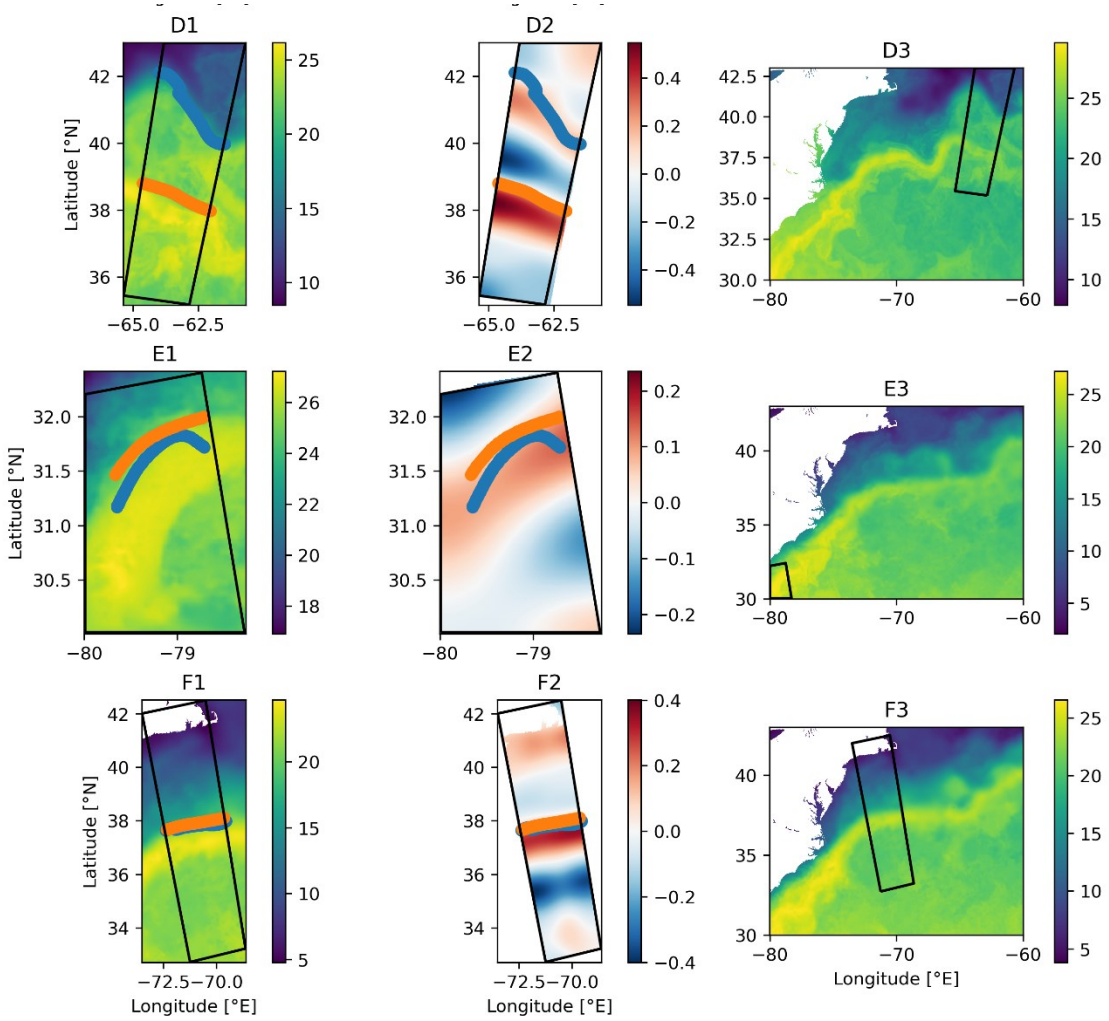

Figure 11. Classification examples using various swaths over the Gulf Stream study region. Column 1 shows the MURSST within the swath's bounding box (°C), column 2 shows the RVL data (m/s), column 3 shows the MURSST over the whole study area (°C), with the black box indicating the location of the RVL swath. Orange lines represent the RVL front, blue lines represent the SST front. D) Misclassification of the ocean current, in this case from the SST image misclassifying an eddy as the current. E) Partial front extraction in both the SST and RVL. F) No issues in extraction, methods worked as intended.

Front Extraction Failures

Because the ocean current can appear in many different forms within the swaths, a method for consistent extraction is difficult to perfect. Variations in the size, shape, thickness, and temperature of the ocean current within the swath, as well as confounding features such as eddies and rings can cause the ridge-finding and feature-identifying methods to fail. Sometimes only a small piece of the current is included within the swath, and in some cases the boundary of a front is diffuse and difficult to demarcate. Human operators can easily distinguish features within images, and use experience to help adjust their predictions, however fronts demarcated by human operators are also somewhat subjective and subject to change, necessitating an automatic extraction for an objective comparison.

Partial extractions occur when the ridge filter is too restrictive, in such as in Figure 11E. An 80^{th} percentile threshold gave the best results in most cases, but when the feature takes up a large portion of the swath, this threshold is too restrictive.

Misclassifications occur when the feature selection algorithm fails to select the ocean current, and instead selects another feature, such as an eddy or ring. Sometimes the extent of the swath only covers a small portion of the ocean current, but a large portion of a ring or eddy. Because the algorithm ranks larger features more highly, a feature with a similar temperature or RVL signature like an eddy or ring could be ranked more highly than a small portion of ocean current. In an operational setting, both these issues could be improved by using the SST and RVL data in tandem, to provide context for each other and select the correct feature using their combined information. However, to prevent contamination between datasets that would affect the comparison, this was not implemented for the purposes of this study.

RVL Failure Angle

Because the RVL data measure the ocean surface velocity towards or away from the sensor, they only capture movement in the range direction. When the ocean current front is perpendicular to the sensor's flight path, it is most clearly visible in the RVL imagery, but when the front is parallel to the flight path, it is not visible. However, the visibility of the signal varies somewhat, regardless of the angle between the ocean current front and sensor heading, because the radial velocity is dependent on the interactions between the wind, waves, and current, as well as the sensor position and look geometry (Chapron et al., 2005), all of which vary between scenes. However, to determine the angle at which this transition from detectable to undetectable generally occurs, the intersection point where an RVL and SST front cross in the RVL failure swaths (Figure 10B) was used to determine the angle of the SST front normal vector of the

ocean current. This normal vector was adjusted by the sensor flight heading angle to determine at what angle, relative to the flight path, the RVL failed to detect the ocean current front (Figure 12). This was calculated for all RVL failure swaths where the fronts intersected and is presented in the results.

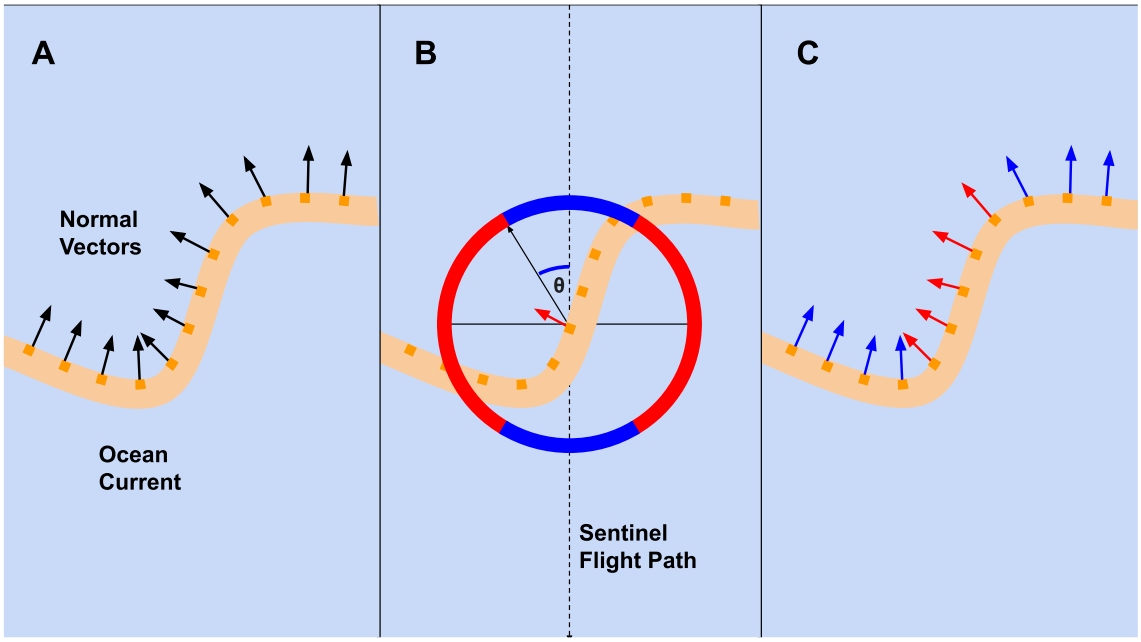

Figure 12. A) Ocean current front with normal vectors at regular intervals. B) Ocean current front with an example normal vector (red) extending outside the range where it is detected (blue arc) by the RVL sensor. C) Ocean current front with all normal vectors coloured according to whether the front is detected in the RVL (blue) or not (red).

SST Failures

The MURSST product is based on MODIS and AVHRR SST data, with auxiliary data from buoys, ships, and microwave sensors used to fill gaps due to cloud cover. However, this coverage is not complete, occasionally resulting in an error sufficient to make part of the ocean current appear colder than the rest of the ocean current, such that it blends in with surrounding water. In these cases, the ocean current appears in the SST data to have gaps (e.g., Figure 10, C1). These gaps can last for long periods of time and occur in multiple places on the ocean currents. While there are several significant periods with gaps, there were only four swaths out of all the swaths for both study areas that overpassed one of these gaps. Two swaths occur on the same day over the GS study region (Figure 13, Figure 14), and the other two occur on different days over the AC study region (Figure 15, Figure 16).

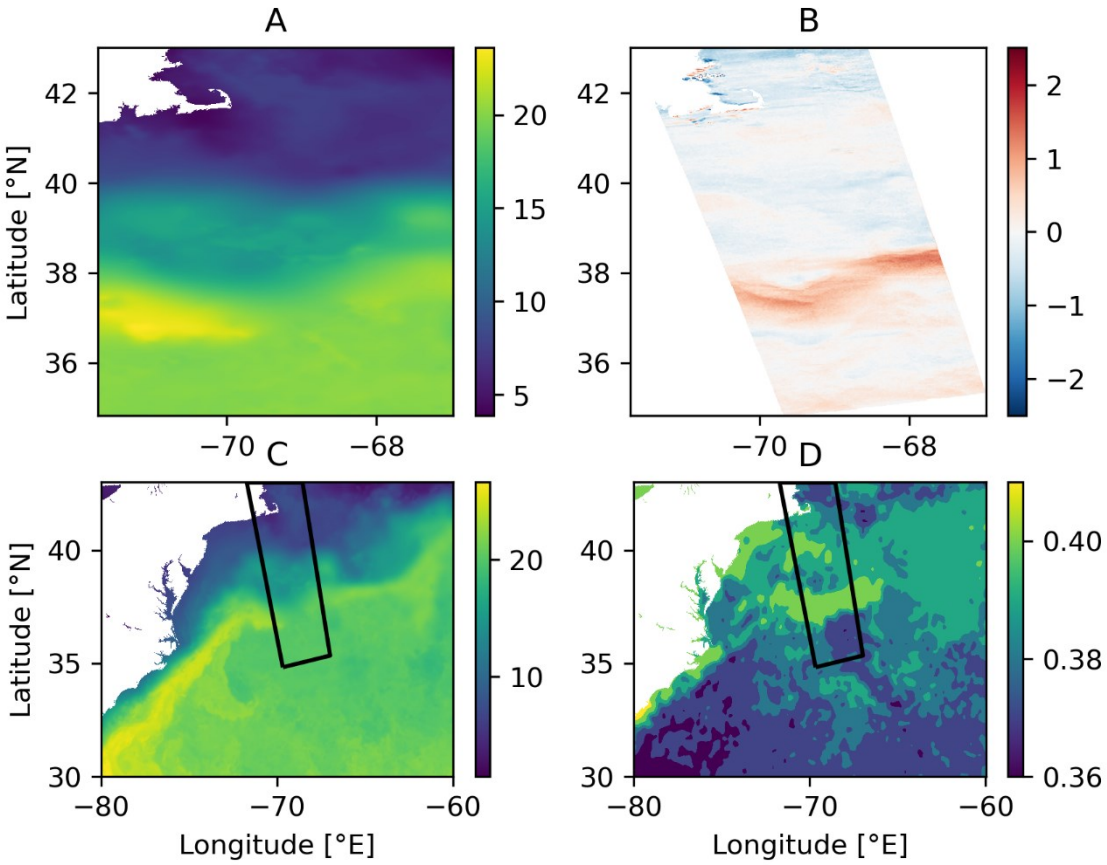

Figure 13. Apparent MURSST failure in the Gulf Stream Study region on the 4th of February 2020. A) The MURSST within the bounding box of the RVL swath in degrees Celsius, showing an apparent gap in the ocean current SST. B) RVL swath from a Sentinel-1A overpass of the Gulf Stream, in meters per second, clearly showing the Gulf Stream in the swath. C) MURSST of the entire study region in degrees Celsius, with the extent of the RVL swath in black. D) MURSST error of the entire study region in degrees Celsius, with the extent of the RVL swath in black.

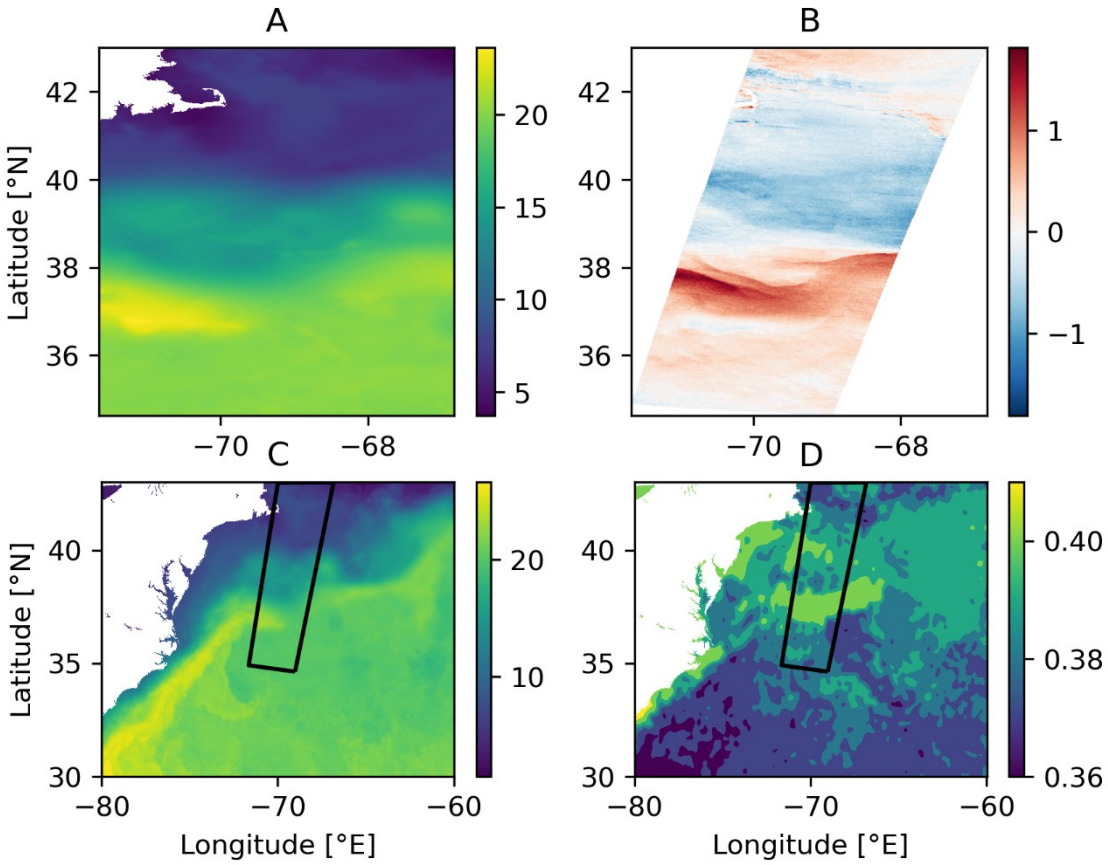

Figure 14. Apparent MURSST failure in the Gulf Stream Study region on the 4th of February 2020. A) The MURSST within the bounding box of the RVL swath in degrees Celsius, showing an apparent gap in the ocean current SST. B) RVL swath from a Sentinel-1B overpass of the Gulf Stream, in meters per second. C) MURSST of the entire study region in degrees Celsius, with the extent of the RVL swath in black. D) MURSST error of the entire study region in degrees Celsius, with the extent of the RVL swath in black.

The swaths that overpassed a noticeable SST failure were both from the 4th of February 2020, taken over the Gulf Stream. The MURSST error in this region is high (Figure 13D, Figure 14D), and the RVL images from Sentinel-1A and Sentinel-1B both show a strong ocean current front signal where the SST gap is present (Figure 13B, Figure 14B), suggesting that the SST in that region is significantly higher than it appears in the MURSST.

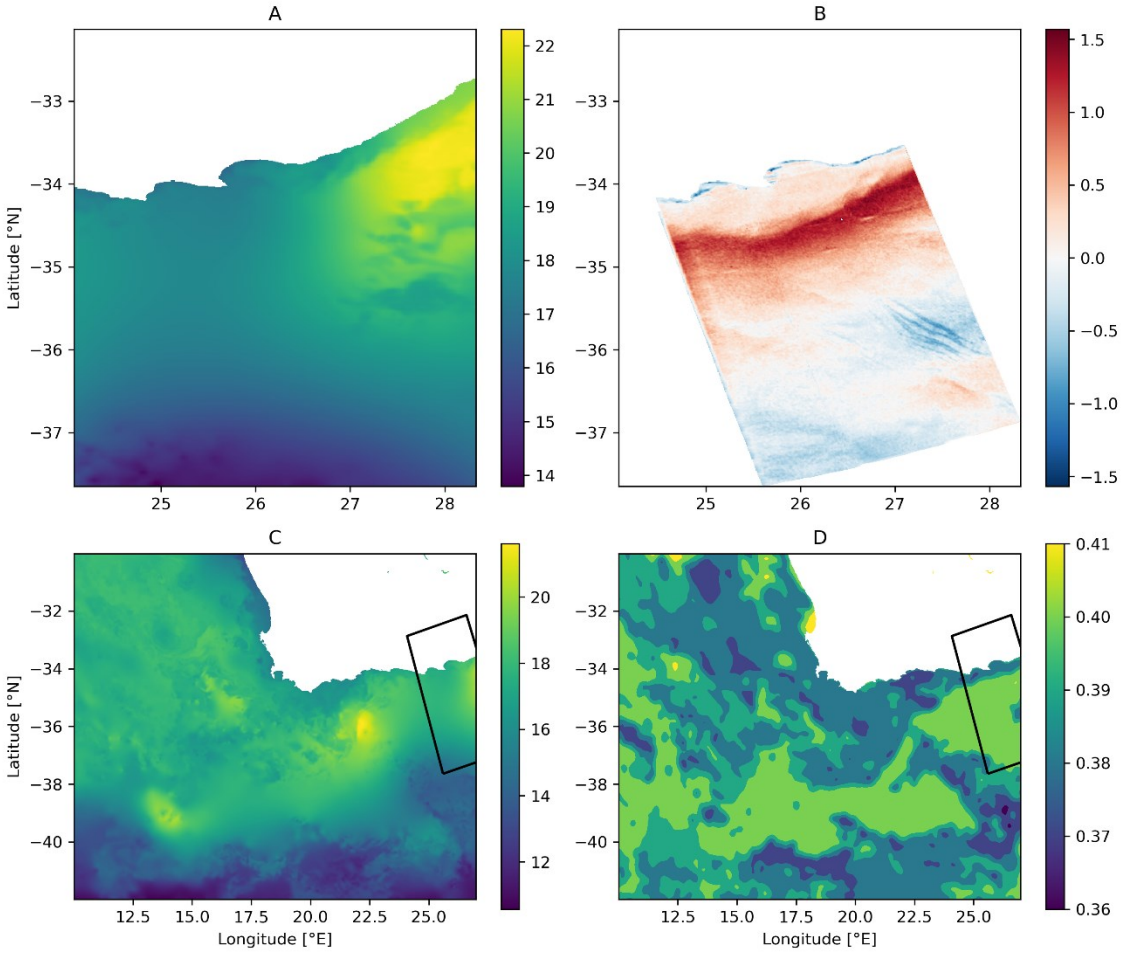

Figure 15. Apparent MURSST failure in the Agulhas Current Study region on the 23rd of July 2020. A) The MURSST within the bounding box of the RVL swath in degrees Celsius, showing an apparent gap in the ocean current SST. B) RVL swath from a Sentinel-1A overpass of the Agulhas Current, in meters per second. C) MURSST of the entire study region in degrees Celsius, with the extent of the RVL swath in black. D) MURSST error of the entire study region in degrees Celsius, with the extent of the RVL swath in black.

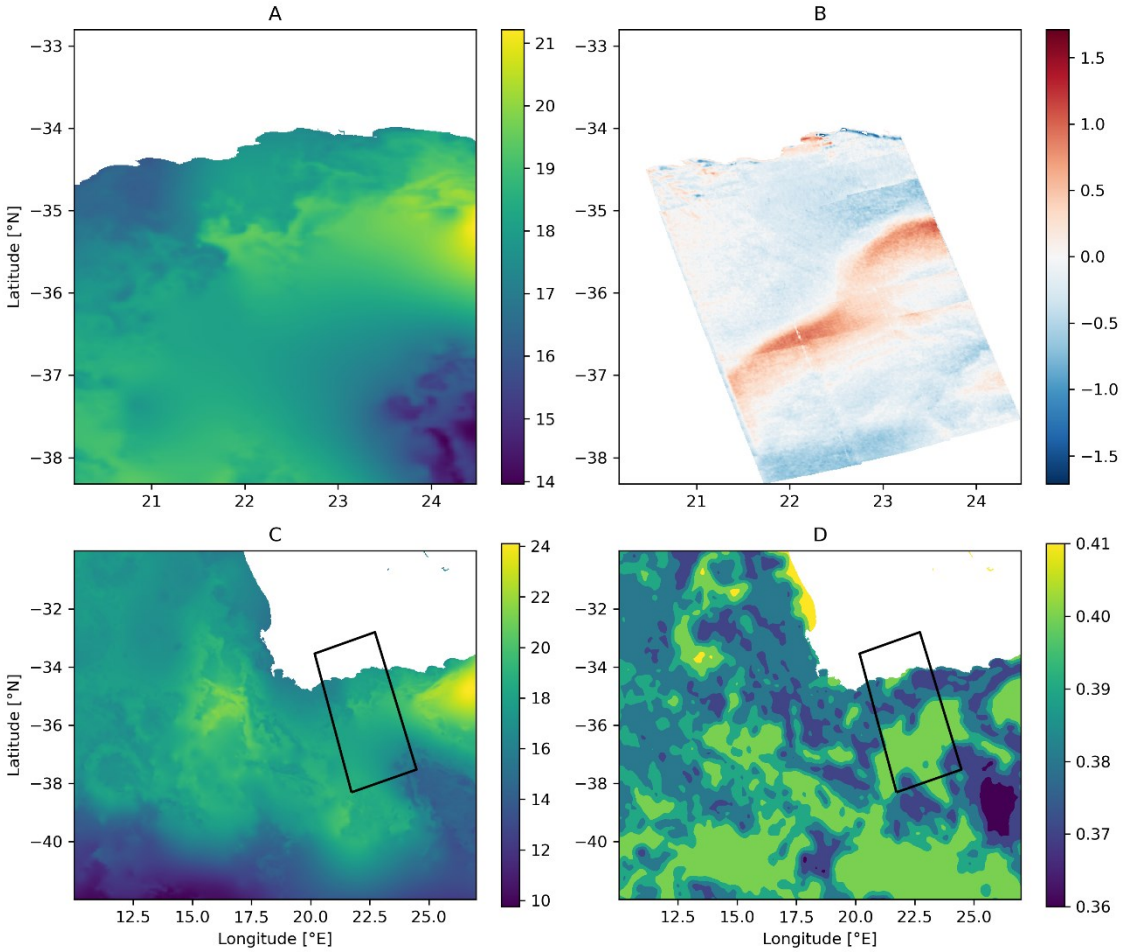

Figure 16. Apparent MURSST failure in the Agulhas Current Study region on the 2nd of August 2020. A) The MURSST within the bounding box of the RVL swath in degrees Celsius, showing an apparent gap in the ocean current SST. B) RVL swath from a Sentinel-1A overpass of the Agulhas Current, in meters per second. C) MURSST of the entire study region in degrees Celsius, with the extent of the RVL swath in black. D) MURSST error of the entire study region in degrees Celsius, with the extent of the RVL swath in black.

The swaths that overpassed a noticeable SST failure in the Agulhas Current study region were both sensed during the southern hemisphere's winter months. The MURSST error over nearly the entire ocean current is high (Figure 15D, Figure 16D), and this is reflected in an unusually low estimated temperature over most of the ocean current. Once again, the RVL images both show a strong ocean current front signal where the SST gap is present (Figure 15D, Figure 16D), suggesting that the SST in that region is significantly higher than it appears in the MURSST.

3. Results

Table 1 provides a summary of the classification results over all swaths.

Table 1. Summary of classification results for the Gulf Stream, Agulhas Current, and the combination of both.

	Gulf Stream	Agulhas Current	Both Regions
Out of Bounds	40	365	405
No issues	252	76	328
RVL failure	35	12	47
SST failure	2	2	4
Combined Successful	289	90	379
Misclassification	93	23	116
Partial	59	23	82
Combined Rejects	152	46	198
Total Swaths	481	136	577

Overall, the methods have a 65% success rate over the GS and AC study regions for outputting the "Combined Successful" fronts pairs (GS: 65%, AC: 66%), which include the "No Issues", "RVL failure", and "SST failure classes". "Out of Bounds" swaths were not included in the "Combined Rejects" but are included in the "Total Swaths". All results except the RVL failure angle were calculated using the "No Issues" class of swaths. All SST failures were shown previously (Figure 13, Figure 14, Figure 15, Figure 16), and the RVL failures were used to calculate the RVL failure angle. The mean RVL failure angle was 41.1°, with a standard deviation of 10.6°.

3.1. Gulf Stream

Of the 252 "Combined Successful" front pairs, 112 had the RTOFS available for that day. Summary statistics of the collected data are presented in Table 2.

Table 2. Summary statistics of "No Issues" swaths in the Gulf Stream study area for the following variables: Hausdorff distance in kilometers and Mean Hausdorff Distance in kilometers for all three front set comparisons, percentage of cloud cover over the SST and RVL fronts, range between minimum and maximum temperature of the SST within the swath in degrees Celsius, and the MURSST analysis error over the SST and RVL fronts in degrees Celsius.

	Mean	Median	Std. Dev.	Minimum	Maximum
RVL-SST HD (km)	25.5	21.6	14.3	7.8	115.0
RVL-SST MHD (km)	10.8	9.1	6.2	2.1	38.0
RTOFS-RVL HD (km)	30.5	22.7	27.7	9.8	185.0
RTOFS-RVL MHD (km)	13.0	11.5	7.6	4.5	50.3
RTOFS-SST HD (km)	29.5	21.0	31.3	8.5	223.4
RTOFS-SST MHD (km)	10.1	8.5	6.3	4.3	44.4
All HD	28.5	21.8	22.4	7.8	223.4
All MHD	11.2	9.5	6.6	2.1	50.3

Temperature Range (°C)	15.5	16.4	4.3	2.4	23.4
Clouds (%)	86.3	95.6	19.9	0.0	100.0
MURSST Error (°C)	0.38	0.39	0.01	0.36	0.40

The mean HD for every pairing of front datasets was less than 31 km, with a mean MHD less than 13 km for every pair of front datasets. Temperature range within the swath averaged 15.5°C but went as low as 2.5°C. Mean cloud proportion over the fronts was very high (86.3%), with some fronts being completely clear or cloudy. The Mean MURSST error was 0.38°C, halfway between the maximum and minimum values.

The centroids of the RVL fronts had a mean offset of 27.3 km from the centroids of the SST fronts, and the RVL centroids were north of the SST's centroids 75% of the time, with a mean heading angle (as a compass heading; measured clockwise from North, starting at 0) from RVL to SST of 164.4 (SSE, 15.6 degrees from a purely northern offset). The mean offset between the RTOFS and RVL centroids was 34.7km, and the RVL centroids were north of the RTOFS centroids 79% of the time with a mean heading from RVL to RTOFS of 176 (S, 4 degrees from a purely northern offset). The mean offset between the RTOFS and SST centroids was 34.1 km, and the RTOFS centroids were north of the SST centroids 40% of the time, with a mean heading from RTOFS to SST of 33.7 (NE), indicating RTOFS centroids have a consistently eastward offset from the SST's centroids.

Both the cloud proportion and temperature range had moderate positive correlations with MURSST error (R values of 0.47 and 0.48 respectively). Temperature range and cloud proportion had a weaker positive correlation (R=0.29). Most front pairs were very cloudy, often completely cloud covered.

3.2 Agulhas Current

Summary statistics of the collected data for the AC are presented in Table 3.

Table 3. Summary statistics of all "No Issues" swaths comparing RVL and SST in the Agulhas Current study area for the following variables: Hausdorff distance in kilometers, normalized Mean Hausdorff distance in kilometers, percentage of cloud cover over the fronts, range between minimum and maximum temperature of the SST within the swath in degrees Celsius, and the MURSST analysis error in degrees Celsius.

	Mean	Median	Std. Dev.	Minimum	Maximum
HD (km)	42.2	37.0	23.0	11.6	116.5
MHD (km)	18.7	15.8	11.0	2.5	71.9
Temperature Range (°C)	7.2	6.9	1.5	4.6	10.8
Clouds (%)	71.6	88.8	32.6	0.0	100.0
MURSST Error (°C)	0.38	0.38	0.01	0.37	0.40

The Agulhas Current study region had a mean HD of 42.2 km, and a mean MHD of 18.2 km. The mean temperature range within the swaths was 7.2°C, about half

that of the GS. The AC study region also had a smaller mean proportion of cloud cover over the fronts than the GS, at 71.6%. The MURSST Error in the AC region was 0.38°C, with a minimum of 0.37°C and maximum of 0.4°C.

The centroids of the RVL fronts had a mean offset of 23.5 km from the centroids of the SST fronts, and the RVL centroids were north of the SST's centroids 73% of the time, with a mean heading angle from the RVL to SST of 156.1 (SSE).

The cloud proportion (R=0.24) has a weak positive correlation with MURSST error, but unlike the GS, temperature range of the swath appears to have no correlation with cloud coverage or MURSST error.

3.3 Combined Study Areas

The mean HD over all front datasets was 31.9 km, and the mean MHD was 13.9 km. The mean centroid offset between the RVL and the SST datasets over all study areas was 25.4 km. The mean centroid offset between the RVL and the RTOFS datasets in the GS study region was 34.7 km.

4. Discussion

Front Similarity

The average HD over all front datasets, representing the largest discrepancy between the fronts, was 31.9 km. The mean MHD, representing the average discrepancy between the fronts, was 13.9 km. These values can be interpreted in the context of the sizes of the study areas, approximately 2,580,000 km^2 for the Gulf Stream region and 2,040,000 km^2 for the Agulhas Current region. These discrepancies can be explained by the factors listed in Figure 7: Length difference, rotational offset, shape difference, and translational offset.

The length differences are negligible, since all fronts are cut to the swath extent, and in almost all cases cross the width of the swath (e.g., Figure 10B, Figure 11C). Rotational offset may be a factor, with differences in the timing and accuracy of the sensing meaning that even if both datasets describe ocean conditions on the same day, the current's position may have fluctuated 10s of kilometers over the course of a day (Xie et al., 2007). A case of a meander changing amplitude over a day is more accurately a difference in shape, but on the scale of the swaths it appears like a change in rotation of the front. The HD measures are particularly sensitive to this case because two fronts departing even slightly in direction can produce large HD and MHD. Based on visual observations of the fronts from each dataset, shape differences between the different datasets appear to be the largest contributor to discrepancies between the RTOFS and the other datasets; the RTOFS meanders more on the scale of the swaths than the relatively flat SST and RVL retrievals; this may be a consequence of the Gaussian smoothing step reducing small scale meanders captured by the RTOFS. It is important to note that any discrepancy in front location attributed to front movement between SST and RVL data acquisitions should not be interpreted as an error on the part of either front extraction, instead the two datasets simply describe the location of the front at different times. Additionally, it is important to note that the RVL acts as a proxy for front position, and the maximum gradient of the SST and the maximum gradient of the RVL front are separate, but related, features.

Front Offset

Between the RTOFS and SST, SST centroids are slightly more likely to appear to the north of the RTOFS fronts, as it did in 60% of the swaths, though based on visual observations it is not a consistent offset, and most of the discrepancy between SST and RTOFS appears to be due to these small-scale shape differences. Because the fronts extracted from RVL and SST data are generally similar due to their common extraction method, the main source of the discrepancy between them appears to be a vertical translational offset. The

RVL front centroids appear consistently to the north of both the SST and RTOFS front centroids by an average of 25.4 km 34.7 km, respectively. This offset may be due to the most intense wave action, visible as the highest intensity radial velocity in the RVL image, being consistently generated *over* the SST front rather than around the ocean current's core (where the highest SST values are found), with reduced wave action near the SST front itself.

The RTOFS centroids generally appear to the east of the SST and RVL, possibly as a result of the small-scale meanders of the RTOFS generally tilting eastwards in the direction of Gulf Stream flow, resulting in a concentration of points to the east and a comparatively eastward centroid.

RVL Failure Angle

Because the RVL senses line-of-sight velocity with respect to the sensor, wave action that does not have large velocity components towards or away from the sensor do not provide a significant signal in an RVL image. The RVL signal from wave action is most visible from fronts that are oriented perpendicularly to the sensor's flight path. For the swaths examined in this study, if the normal vector of the SST front at a given point departed more than 40° from either side of the flight path heading, it is generally no longer sufficiently visible in the RVL image to determine its location. The angle appears to vary slightly between swaths, with a standard deviation of about 10°, probably due to differences in wave conditions and sensor look angles. To compensate for this, a concurrent overpass from a complementary sensor with a different flight path heading could be combined to extend the angular coverage and detect features neither sensor could completely detect alone. This already occurs over the GS with multiple cases of complementary sensing using both S1A (ascending) and S1B (descending). The orbits criss-cross at an approximately 10° to 11° offset from longitudinal lines over the study area, and together could detect the entire ocean current front by covering part of each others failure angle range to form a reduced overall failure angle range.

Correlations

The correlation between cloud coverage and MURSST error is positive, but moderate (Gulf Stream R=0.47, Agulhas Current: R=0.24). This is likely due to auxiliary data from microwave sensors, buoys and ships that help infill gaps in cloudy regions. For this reason, even front extraction from very cloudy regions may agree well with RVL imagery in many cases, and their corresponding HD and MHD are low. However, in the cases of SST failure, where the MURSST had unexpectedly cool gaps that make the ocean current blend in with surrounding water, the four RVL swaths that overpassed these regions all showed a strong front exactly where the ocean current was expected to be (Figure 13D, Figure 14, Figure 15, Figure 16). Figure 17 shows that MURSST error in general is higher over the ocean currents in both study areas,

suggesting RVL would provide both valuable validation data and represent a source of auxiliary data for detecting ocean current positions in regions lacking other data.

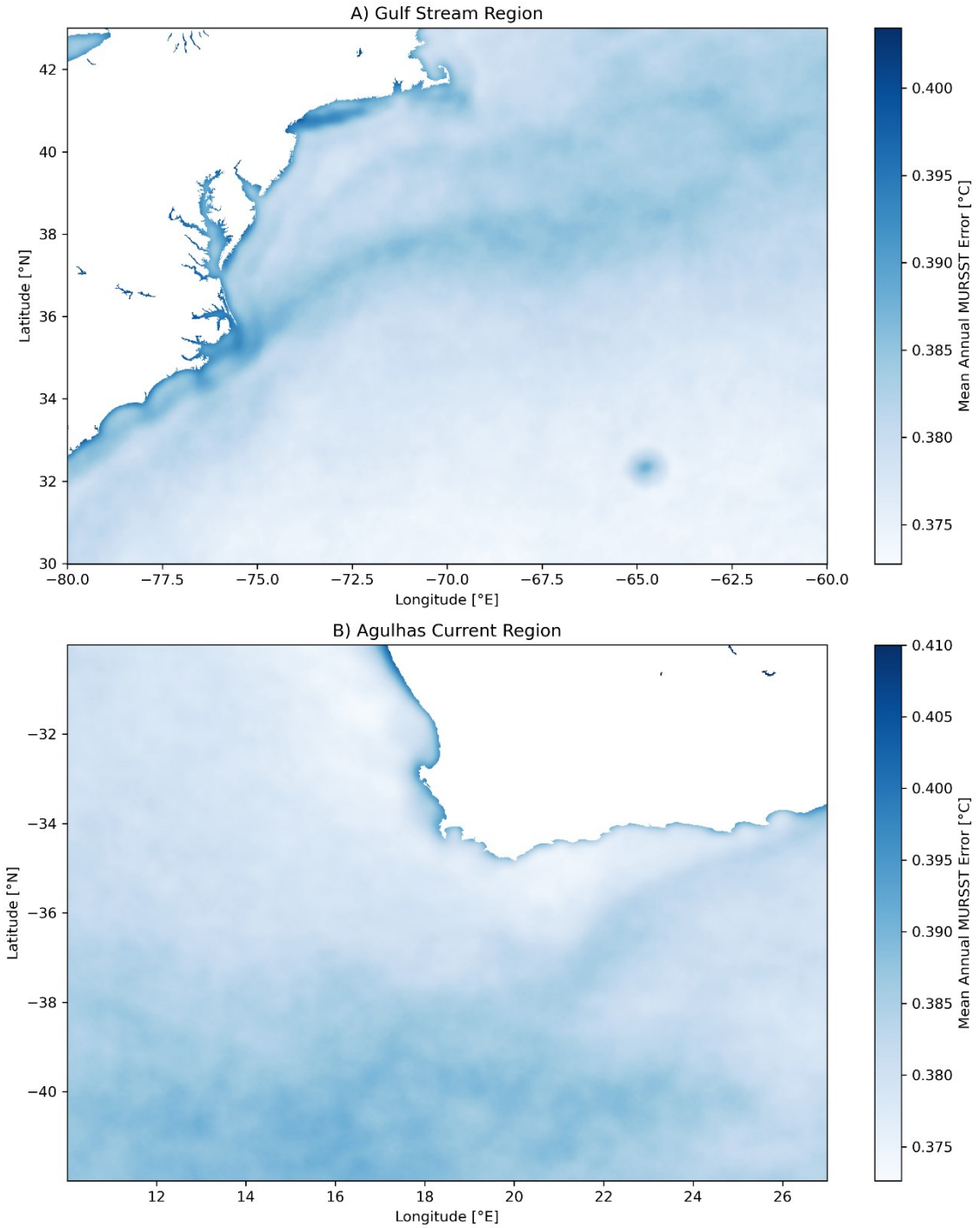

Figure 17. Mean Annual MURSST error in degrees Celsius for A) Gulf Stream study area, and B) the Agulhas Current study area. Note that the MURSST error is generally higher in the vicinity of the ocean currents and coastal regions.

Automatic Front Extraction

The automatic extraction of ocean current fronts represents a challenging task (Jones et al., 2012), but is desirable for speed, consistency, and objectivity. The methods presented here succeeded in automatically extracting ocean current fronts from both RVL and SST images over both study areas 65% of the time. Many of the swaths where the automatic extraction failed had a successful extraction from either the RVL or SST image but not the other, and thus were not suitable for comparison of front locations. There are several potential improvements that could be made that leverage both the SST and RVL datasets together to provide an improved operational product.

Misclassifications could be reduced by finding areas of high confidence in both the RVL and MURSST, if they agree well, then it is likely that the ocean current is there, and if they disagree, it is likely that either one of the positions is a misclassification, or there is a special case such as an RVL or SST failure. Misclassifications could also be reduced by taking a larger sample of properties over multiple years for each study area and using logistic regression to determine a weighted algorithm or creating a neural network to classify the ocean currents. A neural network would have the advantage of being expanded to classify other ocean features such as rings and eddies as well. Partial extractions may be reduced by using an adaptive threshold that is sensitive to the extent of the ocean current within the scene, rather than the fixed 80^{th} percentile threshold used in this study.

Automating the identification of problematic scenes would also be a great improvement over manual classification. In the aforementioned cases where the RVL and MURSST have a large discrepancy, these scenes could be flagged for further analysis, or dealt with using a separate workflow to automatically attempt to identify the problem (e.g., SST failure, RVL failure, misclassification, partial extraction, or other). For example, the algorithm could detect scenes where it is clear from the SST front and sensor heading that the RVL failure angle is exceeded, and automatically flag it as a likely RVL failure. SST failures could be identified via high cloud coverage, high MURSST error, significant SST anomaly, and a clear ocean current front signature in the RVL. Misclassifications would appear as large discrepancies between the SST and RVL front positions, but with the ocean current signal appearing strongly in both images. Partial extractions could be identified by large discrepancies in front length. Finally, recent front locations could be used to help predict the current front location and flag extreme departures from recent front positions.

5. Conclusion

Using a ridge finding algorithm, the northern walls of ocean current fronts were extracted automatically from SST and RVL imagery over the Gulf Stream (GS) and Agulhas Currents (AC) for the year 2020. The swaths were classified manually to determine in which swaths the front extraction succeeded, in which swaths the automatic extraction failed, and in which swaths the RVL and MURSST images themselves failed to detect the ocean current. The automatic extraction algorithm successfully classified fronts 65% of the time over both study areas. The successfully classified fronts were compared using the Hausdorff Distance (HD) and Mean Hausdorff Distance (MHD) functions, which quantified the similarity of the fronts. The mean HD over all fronts of both study regions was 31.9 km (GS: 28.5 km, AC: 42.2 km), and the mean MHD over all fronts was 13.5 km (GS: 11.3 km, AC: 18.7 km), with the HD representing the largest discrepancy between the fronts, and the MHD the average discrepancy. A consistent offset of the RVL centroids to the north of the SST and RTOFS centroids by 25.4 km (averaged over both the GS and AC) and 34.7 km (only the GS had RTOFS data), respectively, was calculated. This offset likely accounts for much of the discrepancy between the fronts, however, slight variations in the shape of the fronts between the datasets, and hourly movements of ocean currents between the sensing times of different datasets also may contribute to the ultimate discrepancies between the fronts. The detection of ocean fronts in RVL data is limited to fronts whose normal angles are within approximately 40° of the sensor's flight heading.

A moderate positive correlation between cloud coverage and MURSST error suggests that the MURSST error increases with cloud coverage, especially in regions where there is no auxiliary data. This is further supported by several cases where the MURSST has a high error and contains a cooler than expected gap where the ocean current is not visible but is clearly apparent in the RVL images. RVL data are thus especially valuable for ocean front location detection in cloudy conditions.

Acknowledgements

The authors would like to thank Todd Spindler (todd.spindler@noaa.gov) and Robert Daniels of the National Oceanic and Atmospheric Administration (NOAA) for sharing the Naval Oceanographic Office (NAVOCEANO) Gulf Stream front positions for 2020. The authors would also like to thank Céline Danilo and Gábor Bella for providing their RVL preprocessing code. Without their contributions this project would not have been possible.

We would also like to acknowledge NOAA's Environmental Research Division's Data Access Program (ERDAAP) for providing the MURSST product, the ESA Copernicus Open Access Hub for providing the Sentinel-1 Ocean

products, as well as Level-1 and Atmosphere Archive & Distribution System Distributed Active Archive Center (LAADS DAAC) for hosting the MODIS cloud mask data.

Author Contributions

Andrew Newall analysed the data and drafted the paper. Anders Knudby and Wesley Van Wychen provided revisions and critical advice on all aspects of the study.

References

Ackerman, S., & Frey, R. (2015). MODIS atmosphere L2 cloud mask product. *NASA MODIS Adaptive Processing System, Goddard Space Flight Center, USA*. http://dx.doi.org/10.5067/MODIS/MOD35_L2.006

Biron, K., Van Wychen, W., & Vachon, P. W. (2018). Gulf Stream Detection from SAR Doppler Anomaly. *Canadian Journal of Remote Sensing*, *44*(4), Article 4. https://doi.org/10.1080/07038992.2018.1516130

Bower, A. S., & Hogg, N. G. (1996). Structure of the Gulf Stream and Its Recirculations at 55°W. *Journal of Physical Oceanography*, *26*(6), 1002–1022. https://doi.org/10.1175/1520-0485(1996)026<1002:SOTGSA>2.0.CO;2

Bulbul, A., Capin, T., Lavoué, G., & Preda, M. (2011). Assessing Visual Quality of 3-D Polygonal Models. *Signal Processing Magazine, IEEE*, *28*, 80–90. https://doi.org/10.1109/MSP.2011.942466

Chapron, B., Collard, F., & Ardhuin, F. (2005). Direct measurements of ocean surface velocity from space: Interpretation and validation. *Journal of Geophysical Research: Oceans*, *110*(C7). https://doi.org/10.1029/2004JC002809

Chassignet, E. P., & Garraffo, Z. D. (2001). *Viscosity Parameterization and the Gulf Stream Separation*. 6.

Chin, T. M., Vazquez-Cuervo, J., & Armstrong, E. M. (2017). A multi-scale high-resolution analysis of global sea surface temperature. *Remote Sensing of Environment*, *200*, 154–169. https://doi.org/10.1016/j.rse.2017.07.029

Danilo, C., & Bella, G. (2018). Extracting Usable Geophysical Doppler Properties from Sentinel–1 for Coastal Monitoring. *2018 Doppler Oceanography from Space (DOfS)*, 1–5. https://doi.org/10.1109/DOfS.2018.8587274

Eiter, T., & Mannila, H. (1994). *Computing discrete Fréchet distance*.

Engen, G., & Johnsen, H. (2015). *Sentinel-1 Doppler and Ocean Radial Velocity Algorithm Definition*. ESA. https://sentinels.copernicus.eu/documents/247904/349449/S1_L2_RVL_AlgoDef_v1+2.pdf

ESA. (2020). *ASF DAAC 2020, contains modified Copernicus Sentinel data 2020, processed by ESA.*

Frangi, A. F., Niessen, W. J., Vincken, K. L., & Viergever, M. A. (1998). Multiscale vessel enhancement filtering. In W. M. Wells, A. Colchester, & S. Delp (Eds.), *Medical Image Computing and Computer-Assisted Intervention—MICCAI'98* (pp. 130–137). Springer. https://doi.org/10.1007/BFb0056195

Gordon, A. L. (1985). Indian-Atlantic transfer of thermocline water at the Agulhas Retroflection. *Science*, *227*, 1030–1034.

Hansen, D. V. (1970). Gulf stream meanders between Cape Hatteras and the Grand Banks. *Deep Sea Research and Oceanographic Abstracts*, *17*(3), Article 3. https://doi.org/10.1016/0011-7471(70)90064-1

Hansen, M. W., Collard, F., Dagestad, K.-F., Johannessen, J. A., Fabry, P., & Chapron, B. (2011). Retrieval of Sea Surface Range Velocities From Envisat ASAR Doppler Centroid Measurements. *IEEE Transactions on Geoscience and Remote Sensing*, *49*(10), Article 10. https://doi.org/10.1109/TGRS.2011.2153864

Huttenlocher, D. P., Klanderman, G. A., & Rucklidge, W. J. (1993a). Comparing images using the Hausdorff distance. *IEEE Transactions on Pattern Analysis and Machine Intelligence*, *15*(9), Article 9. https://doi.org/10.1109/34.232073

Huttenlocher, D. P., Klanderman, G. A., & Rucklidge, W. J. (1993b). Comparing images using the Hausdorff distance. *IEEE Transactions on Pattern Analysis and Machine Intelligence*, *15*(9), Article 9. https://doi.org/10.1109/34.232073

Johannessen, J. A., Chapron, B., Collard, F., Kudryavtsev, V., Mouche, A., Akimov, D., & Dagestad, K.-F. (2008). Direct ocean surface velocity measurements from space: Improved quantitative interpretation of Envisat ASAR observations. *Geophysical Research Letters*, *35*(22), Article 22. https://doi.org/10.1029/2008GL035709

Jones, C. T., Sikora, T. D., Vachon, P. W., & Wolfe, J. (2012). Toward Automated Identification of Sea Surface Temperature Front Signatures in *Radarsat-2* Images. *Journal of Atmospheric and Oceanic Technology*, *29*(1), Article 1. https://doi.org/10.1175/JTECH-D-11-00088.1

Joseph, A. (2014). Oceanic Currents and Their Implications. In *Measuring Ocean Currents* (pp. 1–49). Elsevier. https://doi.org/10.1016/B978-0-12-415990-7.00001-6

Lambhate, D., Sharma, R., Clark, J., Gangopadhyay, A., & Subramani, D. (2021). W-Net: A Deep Network for Simultaneous Identification of Gulf Stream and Rings From Concurrent Satellite Images of Sea Surface Temperature and Height. *IEEE Transactions on Geoscience and Remote Sensing*, 1–13. https://doi.org/10.1109/TGRS.2021.3096202

Lo, H. K., & McCord, M. R. (1995). Routing through dynamic ocean currents: General heuristics and empirical results in the gulf stream region.

Transportation Research Part B: Methodological, *29*(2), 109–124. https://doi.org/10.1016/0191-2615(94)00029-Y

Lutjeharms, J. R. E. (1981). Features of the southern Agulhas Current circulation from satellite remote sensing. *South African Journal of Science*, *77*(5), 231–236.

Lutjeharms, J. R. E. (2006). *The Agulhas Current*. Springer Berlin / Heidelberg. http://ebookcentral.proquest.com/lib/ottawa/detail.action?docID=304665

Min, D., Zhilin, L., & Xiaoyong, C. (2007). Extended Hausdorff distance for spatial objects in GIS. *International Journal of Geographical Information Science*, *21*(4), Article 4. https://doi.org/10.1080/13658810601073315

Minobe, S., Kuwano-Yoshida, A., Komori, N., Xie, S.-P., & Small, R. J. (2008). Influence of the Gulf Stream on the troposphere. *Nature*, *452*(7184), 206–209. https://doi.org/10.1038/nature06690

Moura, R. L., Amado-Filho, G. M., Moraes, F. C., Brasileiro, P. S., Salomon, P. S., Mahiques, M. M., Bastos, A. C., Almeida, M. G., Silva, J. M., Araujo, B. F., Brito, F. P., Rangel, T. P., Oliveira, B. C. V., Bahia, R. G., Paranhos, R. P., Dias, R. J. S., Siegle, E., Figueiredo, A. G., Pereira, R. C., ... Thompson, F. L. (2016). An extensive reef system at the Amazon River mouth. *Science Advances*, *2*(4), e1501252. https://doi.org/10.1126/sciadv.1501252

NASA. (2020, September 15). *Detailed Information for Case PM_MYD_20229_NRT*. https://landweb.modaps.eosdis.nasa.gov/cgi-bin/NRT/displayCase.cgi?esdt=MYD&caseNum=PM_MYD_20229_NRT&caseLocation=cases_data&

NASA/JPL. (2015). *GHRSST Level 4 MUR Global Foundation Sea Surface Temperature Analysis (v4.1)*. NASA Physical Oceanography DAAC. https://doi.org/10.5067/GHGMR-4FJ04

Peloquin, R. (1992). The Navy Ocean Modeling and Prediction Program—From Research to Operations: An Overview. *Oceanography*, *5*(1), 4–8. https://doi.org/10.5670/oceanog.1992.25

Schafer, R. W. (2011). What Is a Savitzky-Golay Filter? [Lecture Notes]. *IEEE Signal Processing Magazine*, *28*(4), Article 4. https://doi.org/10.1109/MSP.2011.941097

Strabala, K. I. (2005). *MODIS cloud mask user's guide*. University of Wisconsin--Madison.

Toggweiler, J. R. (2009). Ocean Circulation: Meridional Overturning Circulation. In J. H. Steele (Ed.), *Encyclopedia of Ocean Sciences (Second Edition)* (pp. 126–131). Academic Press. https://doi.org/10.1016/B978-012374473-9.00596-8

Van Wychen, W., Vachon, P. W., Wolfe, J., & Biron, K. (2018). The Utility of Sentinel-1 Data for Ocean Surface Feature Analysis in the Vicinity of the Gulf Stream. *Canadian Journal of Remote Sensing*, *44*(2), Article 2. https://doi.org/10.1080/07038992.2018.1461558

Xie, L., Liu, X., & Pietrafesa, L. J. (2007). Effect of Bathymetric Curvature on Gulf Stream Instability in the Vicinity of the Charleston Bump. *Journal of Physical Oceanography*, *37*(3), 452–475. https://doi.org/10.1175/JPO2995.1

Zhang, W. G., & Gawarkiewicz, G. G. (2015). Dynamics of the direct intrusion of Gulf Stream ring water onto the Mid-Atlantic Bight shelf. *Geophysical Research Letters*, *42*(18), 7687–7695. https://doi.org/10.1002/2015GL065530

Appendix

Table 4. List of dates where there was an RVL product within the study areas for 2020.

Gulf Stream RVL Dates	Agulhas Current RVL Dates
2020-01-01	2020-01-01
2020-01-02	2020-01-04
2020-01-03	2020-01-08
2020-01-04	2020-01-09
2020-01-05	2020-01-13
2020-01-06	2020-01-16
2020-01-07	2020-01-18
2020-01-08	2020-01-21
2020-01-09	2020-01-25
2020-01-10	2020-01-28
2020-01-11	2020-01-30
2020-01-12	2020-02-02
2020-01-13	2020-02-04
2020-01-14	2020-02-06
2020-01-15	2020-02-09
2020-01-16	2020-02-11
2020-01-17	2020-02-16
2020-01-18	2020-02-18
2020-01-19	2020-02-21
2020-01-20	2020-02-23
2020-01-21	2020-02-26
2020-01-22	2020-02-28
2020-01-23	2020-03-01
2020-01-24	2020-03-06
2020-01-26	2020-03-08
2020-01-27	2020-03-09
2020-01-28	2020-03-11
2020-01-30	2020-03-16
2020-01-31	2020-03-18
2020-02-01	2020-03-21
2020-02-02	2020-03-25
2020-02-03	2020-03-28
2020-02-04	2020-03-30
2020-02-07	2020-04-02
2020-02-08	2020-04-04
2020-02-09	2020-04-06
2020-02-10	2020-04-11
2020-02-11	2020-04-13
2020-02-12	2020-04-14
2020-02-13	2020-04-18

2020-02-14	2020-04-23
2020-02-15	2020-04-26
2020-02-16	2020-04-28
2020-02-17	2020-05-03
2020-02-20	2020-05-05
2020-02-21	2020-05-07
2020-02-22	2020-05-10
2020-02-23	2020-05-12
2020-02-24	2020-05-15
2020-02-25	2020-05-19
2020-02-26	2020-05-22
2020-02-27	2020-05-24
2020-02-28	2020-05-27
2020-02-29	2020-05-31
2020-03-01	2020-06-01
2020-03-02	2020-06-03
2020-03-03	2020-06-05
2020-03-04	2020-06-08
2020-03-05	2020-06-13
2020-03-06	2020-06-15
2020-03-07	2020-06-20
2020-03-08	2020-06-25
2020-03-09	2020-06-29
2020-03-11	2020-07-02
2020-03-12	2020-07-07
2020-03-13	2020-07-09
2020-03-14	2020-07-11
2020-03-15	2020-07-18
2020-03-16	2020-07-19
2020-03-17	2020-07-23
2020-03-18	2020-07-26
2020-03-19	2020-07-28
2020-03-20	2020-08-02
2020-03-21	2020-08-07
2020-03-23	2020-08-09
2020-03-24	2020-08-12
2020-03-25	2020-08-16
2020-03-26	2020-08-19
2020-03-27	2020-08-21
2020-03-28	2020-08-23
2020-03-29	2020-08-26
2020-03-30	2020-08-28
2020-03-31	2020-08-31
2020-04-01	2020-09-04
2020-04-02	2020-09-07

2020-04-04	2020-09-09
2020-04-05	2020-09-14
2020-04-06	2020-09-16
2020-04-07	2020-09-17
2020-04-08	2020-09-19
2020-04-09	2020-09-21
2020-04-10	2020-09-26
2020-04-11	2020-09-28
2020-04-12	2020-09-29
2020-04-13	2020-10-03
2020-04-14	2020-10-10
2020-04-15	2020-10-11
2020-04-16	2020-10-13
2020-04-17	2020-10-18
2020-04-18	2020-10-20
2020-04-19	2020-10-22
2020-04-20	2020-10-23
2020-04-21	2020-10-25
2020-04-22	2020-10-30
2020-04-23	2020-11-01
2020-04-24	2020-11-03
2020-04-25	2020-11-06
2020-04-26	2020-11-11
2020-04-27	2020-11-13
2020-04-28	2020-11-15
2020-04-29	2020-11-18
2020-04-30	2020-11-20
2020-05-01	2020-11-23
2020-05-02	2020-11-25
2020-05-03	2020-11-27
2020-05-04	2020-11-30
2020-05-05	2020-12-02
2020-05-06	2020-12-05
2020-05-07	2020-12-09
2020-05-08	2020-12-12
2020-05-09	2020-12-14
2020-05-10	2020-12-17
2020-05-11	2020-12-21
2020-05-13	2020-12-22
2020-05-14	2020-12-24
2020-05-15	2020-12-26
2020-05-16	
2020-05-17	
2020-05-18	
2020-05-19	

2020-05-20	
2020-05-22	
2020-05-23	
2020-05-24	
2020-05-25	
2020-05-26	
2020-05-27	
2020-05-28	
2020-05-29	
2020-05-30	
2020-05-31	
2020-06-01	
2020-06-02	
2020-06-03	
2020-06-04	
2020-06-06	
2020-06-07	
2020-06-08	
2020-06-09	
2020-06-10	
2020-06-11	
2020-06-12	
2020-06-13	
2020-06-14	
2020-06-15	
2020-06-17	
2020-06-18	
2020-06-19	
2020-06-20	
2020-06-21	
2020-06-22	
2020-06-23	
2020-06-24	
2020-06-25	
2020-06-26	
2020-06-27	
2020-06-28	
2020-06-30	
2020-07-01	
2020-07-02	
2020-07-03	
2020-07-04	
2020-07-05	
2020-07-06	
2020-07-07	

2020-07-08	
2020-07-09	
2020-07-10	
2020-07-12	
2020-07-13	
2020-07-14	
2020-07-15	
2020-07-16	
2020-07-17	
2020-07-18	
2020-07-19	
2020-07-20	
2020-07-21	
2020-07-22	
2020-07-23	
2020-07-24	
2020-07-25	
2020-07-26	
2020-07-28	
2020-07-29	
2020-07-30	
2020-08-01	
2020-08-02	
2020-08-03	
2020-08-04	
2020-08-05	
2020-08-06	
2020-08-07	
2020-08-08	
2020-08-09	
2020-08-10	
2020-08-11	
2020-08-12	
2020-08-13	
2020-08-14	
2020-08-15	
2020-08-16	
2020-08-17	
2020-08-18	
2020-08-19	
2020-08-20	
2020-08-21	
2020-08-22	
2020-08-23	
2020-08-24	

2020-08-25	
2020-08-26	
2020-08-27	
2020-08-28	
2020-08-29	
2020-08-30	
2020-08-31	
2020-09-01	
2020-09-02	
2020-09-03	
2020-09-04	
2020-09-05	
2020-09-06	
2020-09-07	
2020-09-08	
2020-09-09	
2020-09-10	
2020-09-11	
2020-09-12	
2020-09-13	
2020-09-14	
2020-09-15	
2020-09-16	
2020-09-17	
2020-09-18	
2020-09-19	
2020-09-20	
2020-09-21	
2020-09-22	
2020-09-23	
2020-09-24	
2020-09-25	
2020-09-26	
2020-09-27	
2020-09-28	
2020-09-29	
2020-09-30	
2020-10-01	
2020-10-02	
2020-10-03	
2020-10-04	
2020-10-05	
2020-10-06	
2020-10-07	
2020-10-08	

2020-10-09	
2020-10-10	
2020-10-11	
2020-10-12	
2020-10-13	
2020-10-14	
2020-10-15	
2020-10-16	
2020-10-17	
2020-10-18	
2020-10-19	
2020-10-20	
2020-10-21	
2020-10-22	
2020-10-23	
2020-10-24	
2020-10-25	
2020-10-26	
2020-10-28	
2020-10-29	
2020-10-30	
2020-10-31	
2020-11-01	
2020-11-02	
2020-11-03	
2020-11-04	
2020-11-05	
2020-11-06	
2020-11-07	
2020-11-08	
2020-11-09	
2020-11-10	
2020-11-11	
2020-11-12	
2020-11-13	
2020-11-14	
2020-11-15	
2020-11-16	
2020-11-17	
2020-11-18	
2020-11-19	
2020-11-20	
2020-11-21	
2020-11-22	
2020-11-23	

2020-11-24	
2020-11-25	
2020-11-26	
2020-11-27	
2020-11-28	
2020-11-29	
2020-11-30	
2020-12-02	
2020-12-03	
2020-12-04	
2020-12-05	
2020-12-06	
2020-12-07	
2020-12-08	
2020-12-09	
2020-12-10	
2020-12-11	
2020-12-12	
2020-12-13	
2020-12-14	
2020-12-15	
2020-12-16	
2020-12-17	
2020-12-18	
2020-12-19	
2020-12-20	
2020-12-21	
2020-12-22	
2020-12-23	
2020-12-24	
2020-12-25	
2020-12-26	
2020-12-27	
2020-12-28	
2020-12-29	
2020-12-30	
2020-12-31	

Chapter 4

Thesis Conclusion

Ocean currents are critical to the earth's climate and the myriad systems that are linked to it. Weather prediction, optimal shipping routes, and fishery productivity are just a few human concerns intimately linked with the position of ocean currents. From a monitoring perspective, keeping accurate records of fluctuations in ocean current positions is important to catching anomalous movements that may arise as a result of the earth's changing climate. This thesis examined the efficacy of RVL imagery at detecting ocean current fronts as compared to contemporary SST based methods, which are sensitive to the extensive cloud cover that covers ocean currents most of the time.

Using a ridge filter, ocean current front features were extracted from SST and RVL imagery over the Gulf Stream and Agulhas Current for 2020. The derived fronts were compared using similarity metrics and information regarding cloud cover and SST error were gathered. The swaths were classified manually to determine in which swaths the front extraction succeeded, in which swaths the automatic extraction failed, and in which swaths the RVL and MURSST images themselves failed to detect the ocean current.

The successfully classified fronts were compared using the Hausdorff Distance (HD) and Mean Hausdorff Distance (MHD) functions, which quantified the similarity of the fronts. The mean HD over all fronts of both study regions was 31.9 km (GS: 28.8 km, AC: 42.2 km), and the mean MHD over all fronts was 13.5 km (GS: 11.3 km, AC: 18.7 km), with the HD representing the largest discrepancy between the fronts, and the MHD the average discrepancy. A consistent offset of the RVL centroids to the north of the SST and RTOFS centroids by about 25 km likely accounts for much of the discrepancy between the fronts, however, slight variations in shape of the fronts between the datasets and movement of the currents between sensing of the datasets also contribute to the similarity of the fronts. The RVL's detection of ocean current fronts is limited to features where normal angles are generally within 40° of the sensor's flight heading.

A moderate positive correlation between cloud coverage and MURSST error suggested that the MURSST error increases with cloud coverage where there is no auxiliary data. This is further supported by several cases where the MURSST has a high error and contains a cooler than expected gap where the ocean current is not visible but is clearly apparent in the RVL images. This thesis found that RVL is an effective method of detecting ocean features close to perpendicular to the azimuthal flight direction of Sentinel-1 (and future RVL products), including

in cloudy areas where SST-based methods have larger errors and sometimes fail completely.

In future studies, several steps could be made to further improve the estimation of front positions using RVL and SST datasets. The offset between RVL and SST fronts could be better understood by studying cloud-free scenes in which fronts are clearly depicted in both data sets; because such scenes are rare this would likely take several years worth of observations for a study area such as the GS. The cause of the offset would ideally be determined via a study of several clear sky RVL/SST front pairs along with accurate, concurrent sea surface temperature and velocity fields for validation. A simple correction for the offset could be done using a translation based on the average offset with an uncertainty related to its standard deviation, but a more sophisticated correction might use a geophysical model to estimate surface dynamics and uncover its relationship to the front location offset.

In an operational setting, RVL and SST data can be used in tandem to compensate for the shortcomings of both, and to provide higher confidence in the positions of fronts. The RVL derived fronts can be used both to confirm the position of fronts derived from SST data, and to provide more accurate front positions where other auxiliary data is not available. Large differences in estimated front locations could be automatically flagged and manually observed to see if the RVL, SST, or front extraction method is at fault, or automatically processed using additional methods.

The front position could be represented as a confidence interval raster; cells with highest confidence would be those closest to the predicted position of the RVL and MURSST predicted fronts. The northerly offset of the RVL could be compensated for by a simple translation by the mean offset, with a wider confidence interval related to the offset standard deviation to account for the uncertainty of its exact offset. A data coverage layer could be created that combines the known coverage of the input datasets of the MURSST (e.g., MODIS, AVHRR, AMSR2, iQuam) or similar SST ocean model. In cloudy areas that lack auxiliary data coverage, and regions where the MURSST error is high, the front position given by the RVL would be given more weight. This confidence interval raster could be refined over time as new sensors and datasets become available.

As newer and more sophisticated SAR sensors become available, the coverage and resolution of RVL images will increase, improving the accuracy and coverage RVL-derived ocean fronts. For example, the NASA-ISRO Synthetic Aperture Radar (NISAR), set to launch in 2024, will have dual frequency radar, with a higher maximum resolution than Sentinel-1 and the same repeat cycle. Combined with continued Sentinel-1 coverage, other contemporary SAR sensors such as the Radarsat Constellation Mission, as well as the upcoming launch of Sentinel-1C and Sentinel-1D, the utility of RVL data will continue to grow in value over time.